



Discovery and resistance mechanism of a selective CDK12 degrader

Baishan Jiang^{1,2,8}, Yang Gao^{1,2,8}, Jianwei Che^{1,2,8}, Wenchao Lu^{1,2}, Ines H. Kaltheuner³, Ruben Dries^{1,4,5}, Marian Kalocsay^{1,6}, Matthew J. Berberich⁶, Jie Jiang^{1,2}, Inchul You^{1,2}, Nicholas Kwiatkowski^{1,2}, Kristin M. Riching⁷, Danette L. Daniels^{1,7}, Peter K. Sorger^{1,6}, Matthias Geyer³, Tinghu Zhang^{1,2}✉ and Nathanael S. Gray^{1,2}✉

Cyclin-dependent kinase 12 (CDK12) is an emerging therapeutic target due to its role in regulating transcription of DNA-damage response (DDR) genes. However, development of selective small molecules targeting CDK12 has been challenging due to the high degree of homology between kinase domains of CDK12 and other transcriptional CDKs, most notably CDK13. In the present study, we report the rational design and characterization of a CDK12-specific degrader, BSJ-4-116. BSJ-4-116 selectively degraded CDK12 as assessed through quantitative proteomics. Selective degradation of CDK12 resulted in premature cleavage and poly(adenylation) of DDR genes. Moreover, BSJ-4-116 exhibited potent antiproliferative effects, alone and in combination with the poly(ADP-ribose) polymerase inhibitor olaparib, as well as when used as a single agent against cell lines resistant to covalent CDK12 inhibitors. Two point mutations in CDK12 were identified that confer resistance to BSJ-4-116, demonstrating a potential mechanism that tumor cells can use to evade bivalent degrader molecules.

CDKs are serine/threonine protein kinases that play major roles in regulating many different aspects of mammalian cellular function, most notably cell cycle and transcription¹. Most transcriptional CDKs^{2–5} (CDK7, CDK9, CDK11, CDK12 and CDK13) catalyze multiple phosphorylation events on the C-terminal domain (CTD) of RNA Pol II, a region of Pol II that consists of 52 heptapeptide (TyrSerProThrSerProSer) repeats. The pattern of phosphorylation of the CTD serves to regulate multiple aspects of transcription and post-transcriptional events. For example, CDK9-dependent phosphorylation of Ser2 in a Pol II CTD repeat sequence is responsible for the transition from transcription initiation to productive elongation and genetic depletion of CDK9 leads to a global downregulation of transcription⁶. On the other hand, in addition to regulating elongation, CDK12 phosphorylation of Ser2 sites on the 3'-end of genes was shown to be important for transcription termination and RNA processing⁷. The genetic loss of CDK12 results in a selective transcriptional defect for genes involved in cellular response to DNA damage, stress and heat shock^{8–10}. CDK12 silencing and the use of a selective, covalent CDK12/-13 inhibitor THZ531 (1) resulted in repression of DDR-associated genes, such as *BRCA1* and *ATR*^{11–13} (Extended Data Fig. 1a), by inducing usage of intronic poly(adenylation), a process that produces truncated messenger RNA isoforms and results in aberrant protein production.

The genomic instability induced by CDK12 inactivation might provide an opportunity for cancer therapy. For example, ovarian and triple-negative breast cancer cells with the lower expression of CDK12 are more sensitive to the poly(ADP-ribose) polymerase (PARP) inhibitor olaparib, and a combination treatment of olaparib and dinaciclib, a nonselective CDK12 inhibitor, synergistically suppressed tumor growth in PDX models^{14,15}. In metastatic osteo-

sarcoma, CDK12 inhibition sufficed to prevent lung colonization in ex vivo models with low *MYC* expression¹⁶. In addition, CDK12 inhibition exhibits synthetic lethality in other genetic or cellular contexts, for example, *MYC* dependency^{7,17}, CHK1 inhibition¹⁸ and EWS/FLI rearrangement^{11,15}. This suggests that CDK12 directed targeted therapy, especially when combined with agents that inhibit DNA-repair processes, and selective CDK12 inhibitors would be valuable as both research tools and experimental therapeutics.

Currently available small-molecule inhibitors cannot differentiate CDK12 and the closely related CDK13, because their ATP-binding sites are essentially identical^{19–23}. Although CDK12 and CDK13 are thought to be functionally redundant in some capacities, such as their ability to phosphorylate Ser2 of Pol II (ref. ²⁴), recent studies indicate that these kinases regulate transcription of distinct gene subsets^{25,26}. Therefore, small molecules that selectively target CDK12 are needed to elucidate the biological functions of CDK12 and validate its therapeutic potential. Inspired by our recent success in developing selective degraders for closely related, cell-cycle regulatory CDKs (CDK4 and CDK6), and a transcriptional CDK (CDK9)^{27–29}, we examined whether this strategy can be used to achieve selective CDK12 degradation. In the present study, we report the discovery of the first selective CDK12 degrader, BSJ-4-116 (2). We show that BSJ-4-116 downregulates the expression of DDR genes and exhibits antiproliferative activity in cancer cells. We also demonstrate that CDK12 degradation alone or in combination with PARP inhibitors could be a therapeutic avenue for targeting the intrinsic genomic instability in a T-cell acute lymphoblastic leukemia (T-ALL) model. Importantly, although BSJ-4-116 overcomes resistance toward existing covalent inhibitors, we report that chronic exposure leads to acquired resistance to this

¹Department of Cancer Biology, Dana-Farber Cancer Institute, Boston, MA, USA. ²Department of Biological Chemistry and Molecular Pharmacology, Harvard Medical School, Boston, MA, USA. ³Institute of Structural Biology, University of Bonn, Bonn, Germany. ⁴Department of Hematology and Oncology, Boston University, Boston, MA, USA. ⁵Department of Computational Medicine, Boston University, Boston, MA, USA. ⁶Laboratory of Systems Pharmacology, Harvard Medical School, Boston, MA, USA. ⁷Promega Corporation, Madison, WI, USA. ⁸These authors contributed equally: Baishan Jiang, Yang Gao, Jianwei Che. ✉e-mail: tinghu_zhang@dfci.harvard.edu; nathanael_gray@dfci.harvard.edu

compound through CDK12 mutation. These observations have important implications for degrader development, especially given that a proposed benefit of this class of degrader molecules is the ability to overcome resistance and minimize/abolish the rate at which drug resistance emerges^{30–34}.

Results

Design of a selective CDK12 degrader BSJ-4-116. The most common degrader molecules incorporate two molecular handles, one that recognizes and binds the protein of interest and one that binds an E3 ubiquitin ligase. The two handles are typically connected via a linker. Development of a successful degrader molecule usually requires optimization of the linker length, position and composition, selection of the appropriate target binder and E3 ligase, and empirical screening for cell penetration, ternary complex formation and target degradation^{35–37}. To rationally design a selective CDK12 degrader, we first analyzed the protein plasticity of the CDK12/-13 kinase domain in available crystal structures (Protein Data Bank (PDB) accession nos. of CDK12: 5ACB, 6CKX and 6B3E; PDB accession no. of CDK13: 5EFQ). We found that CDK12 has a higher conformational flexibility than CDK13 at the C-terminal tail, a CDK12/-13 feature that is known to interact with ATP-competitive inhibitors. We thus hypothesized that CDK12 has a higher tolerability than CDK13 with respect to the exit vector for linker attachment and degrader design. This suggested that CDK12-selective degrader might be achievable. Our starting point for CDK12-selective degrader design was the THZ531 scaffold, which is a dual CDK12/-13 covalent inhibitor¹⁹. We dissected THZ531 into three fragments (3–5) that were profiled for CDK12 binding by induced-fit docking. As shown in Extended Data Fig. 1a, fragment 5 was suggested as the most efficient ligand (-0.41 ligand efficiency score). This predicted efficiency for fragment 5 was confirmed in biochemical assay (half-maximal inhibitory concentration, $IC_{50}=107\text{ nM}$; Extended Data Fig. 1b). Based on the predicted binding pose for fragment 5, we chose the piperidine moiety as the exit vector for installing the linker, followed by a ligand that has been extensively used to recruit cereblon (CRBN), an E3 ubiquitin ligase. A series of degrader molecules (6–12) was synthesized (Fig. 1a and Supplementary Table 1), and a primary screen by western blotting led to identification of BSJ-4-23 as a potent CDK12 degrader (Extended Data Fig. 1c). A dose titration of BSJ-4-23 in Jurkat cells revealed notable degradation of CDK12 at 250 nM whereas, with the same concentration, CDK13 protein level was minimally affected (Fig. 1b).

We reasoned that the selectivity of BSJ-4-23 for CDK12 might be attributed to a failure to form a CRBN/BSJ-4-23/CDK13 ternary complex. To probe this possibility, we used computational modeling to generate the ternary complex structures of CDK12 and CDK13 with the degrader molecule and CRBN. BSJ-4-23 was found to fit tightly in the grooves between CDK12 and CRBN proteins and induces a complementary protein–protein interaction (PPI) (Extended Data Fig. 1d). By examining the putative PPI interface, we identified several possible key contributing factors to observed selective degradation of CDK12. As shown in Fig. 1c, we noted that CDK12 Lys745 is located within a hydrogen bond distance from CRBN Cys394, whereas a corresponding residue in CDK13 (Arg723) disfavors the conformation with CRBN as indicated by the partial molecular surface overlapping between Arg723 of CDK13 and the nearby residues of CRBN. Importantly, as indicated by the residue surface of Arg723 (gray surface), CDK13 Met730 (yellow surface) was limiting the conformational space for the Arg723 side chain through close contact and reinforcing the steric repulsion between CDK13 and CRBN. The model of the ternary complexes suggests that the (R)-3-aminopiperidine position may represent a ‘privileged’ exit vector position of CRBN-based degraders for CDK12, which might be transferable to other scaffolds. Therefore, we modified the ligand that was used for a promiscuous

multi-kinase degrader molecule TL12-186 (13)³⁸ by replacing the 4-(piperazin-1-yl)aniline with (R)-3-aminopiperidine to generate BSJ-4-116 and a negative control BSJ-4-116-NC (14), in which the glutarimide nitrogen was methylated to block binding to CRBN²⁹ (Fig. 1d). As expected, BSJ-4-116 demonstrated a low nanomolar IC_{50} for inhibiting CDK12 enzymatic activity (Extended Data Fig. 1b) and exhibited potent CDK12 degradation in Jurkat cells in a dose- and time-dependent manner, whereas CDK13 protein level was minimally affected (Fig. 1e and Extended Data Fig. 1e). BSJ-4-116 also substantially suppressed the phosphorylation of Pol II Ser2 and Thr4, whereas p-Ser5 and p-Ser7 were not inhibited. Surprisingly, contrary to the report that CDK12 depletion by small interfering RNA leads to cyclin K degradation³⁹, BSJ-4-116-induced CDK12 degradation did not affect the cyclin K protein level. As expected, BSJ-4-116-NC and THZ531 had no effect on the levels of CDK13 and cyclin K (Fig. 1e). The CDK12 degradation induced by BSJ-4-116 was fully rescued by pretreatment with carfilzomib (a proteasome inhibitor), MLN4924 (a neddylation inhibitor that prevents CRBN activity by removing a critical post-translational modification needed for CRBN function), CDK12 covalent inhibitor THZ531 (competes for degrader binding on the target) and the CRBN ligand thalidomide (competes for degrader binding on the E3 ligase side; Extended Data Fig. 1f). In addition, the rescue could also be realized through a genetic deletion of CRBN in Jurkat cells (Extended Data Fig. 1f). To determine the selectivity for kinase binding, we performed KINOMEscan profiling at a concentration of 1 μM across a panel of 468 human kinases. BSJ-4-116 exhibited highly selective kinase profile, with an S-score (10) value of 0.017 (Extended Data Fig. 1g and Supplementary Dataset 2). The selectivity for degradation was assessed by proteome-wide profiling using Jurkat cells that were treated with 50 nM BSJ-4-116 for 8 h, then subjected to a multiplexed mass spectrometry (MS)-based proteomic analysis. These experiments detected CDK12 as the only kinase that was significantly degraded (by fourfold) (Fig. 1f and Extended Data Fig. 1h). To understand the degrader selectivity for CDK12 over CDK13, we also utilized NanoBRET, live cell, ternary complex assays to monitor ternary complex formation. A robust ternary complex was induced between CDK12 and CRBN with BSJ-4-116, but not BSJ-4-116-NC, and no appreciable ternary complex formation was observed between CDK13 with CRBN on BSJ-4-116 treatment. As suggested by the computational model, a reduced ternary complex was observed between CRBN and either single mutant or double mutant of Lys745Leu, Leu752Met compared with wild-type CDK12. It is interesting that a single mutant of Met730Leu or double mutant with Arg723Lys on CDK13 enhanced ternary complex formation with CRBN relative to wild-type CDK13, although Arg723Lys mutant alone did not show an appreciable ternary complex with CRBN (Extended Data Fig. 1i). Taken together, those findings demonstrated that BSJ-4-116-induced CDK12 degradation is proteasome and CRBN dependent through efficient ternary complex formation, while sparing the closely related kinase CDK13.

BSJ-4-116 regulates DDR genes via poly(adenylation). The regulation of DDR genes by CDK12 has been well documented using genetic knockdown and small-molecule inhibitors such as THZ531 (refs. ^{9,13}). To compare the pharmacological effects of our degrader molecule with those of an inhibitor, we performed 3'-poly(A) sequencing in Jurkat cells exposed to BSJ-4-116, BSJ-4-116-NC or THZ531 (Extended Data Fig. 2a). A concentration of 50 nM or 250 nM was chosen for BSJ-4-116 and THZ531, respectively, and an 8-h exposure time point to allow time for almost complete CDK12 degradation (Extended Data Fig. 2b). As shown in Fig. 2a, the changes in gene expression due to treatment with THZ531 and BSJ-4-116 were highly correlated (Pearson's $r=0.82$, $R^2=0.67$) and resulted predominantly in decreased expression

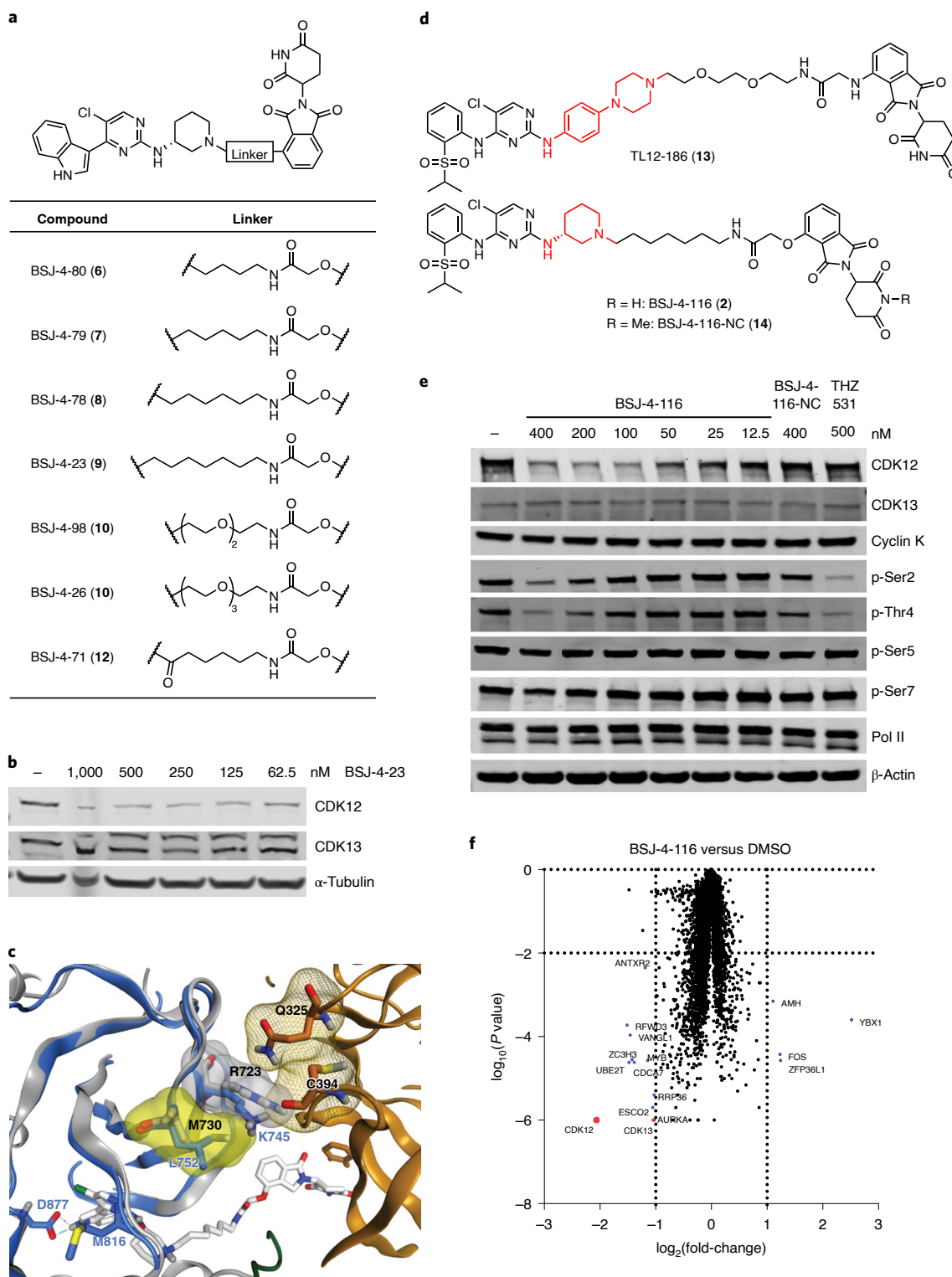


Fig. 1 | Development and characterization of CDK12 degrader BSJ-4-116. **a**, Chemical structures of CDK12 degraders derived from fragment **5** (Extended Data Fig. 1). **b**, Western blots for CDK12, CDK13 and α -tubulin in Jurkat cells after 6 h of treatment with DMSO and BSJ-4-23 at indicated nanomolar concentrations. Data represent $n=2$ independent experiments. **c**, Superposition of CDK13 with modeled CDK12/BSJ-4-23/CRBN ternary complex (CDK12 in blue, PDB accession no. 5ACB; CDK13 in gray, PDB accession no. 5EFQ; BSJ-4-23 carbons in light gray; CRBN in orange, PDB accession no. 4TZ4). The gray and yellow transparent surfaces are for Arg723 and Met730 of CDK13, respectively. The orange mesh is for Gln325 and Cys394 in CRBN. **d**, Chemical structures of a promiscuous kinase degrader TL12-186, a CDK12 degrader BSJ-4-116 ($R=H$) and its negative control BSJ-4-116-NC ($R=Me$). **e**, Immunoblots for CDK12, CDK13, cyclin K, p-Ser2, p-Thr4, p-Ser5, p-Ser7, Pol II and β -actin in Jurkat cells after 6 h of treatment with DMSO, BSJ-4-116, BSJ-4-116-NC and THZ531 at the indicated concentrations. Data represent $n=2$ independent experiments. **f**, Proteome-wide selectivity of BSJ-4-116. Quantitative proteomics show relative abundance of proteins measured by multiplexed quantitative MS-based proteomics in Jurkat cells treated for 8 h with BSJ-4-116 (50 nM) or vehicle (DMSO). CDK12 and CDK13 are marked in red. Proteins marked in blue are a group of nonkinases affected by BSJ-4-116. Dotted lines indicate the threshold for statistically significantly degraded proteins ($\log_{10}(P \text{ value}) < -2$ and $\log_2(\text{fold change}) < -1$). Data are from $n=3$ biologically independent samples.

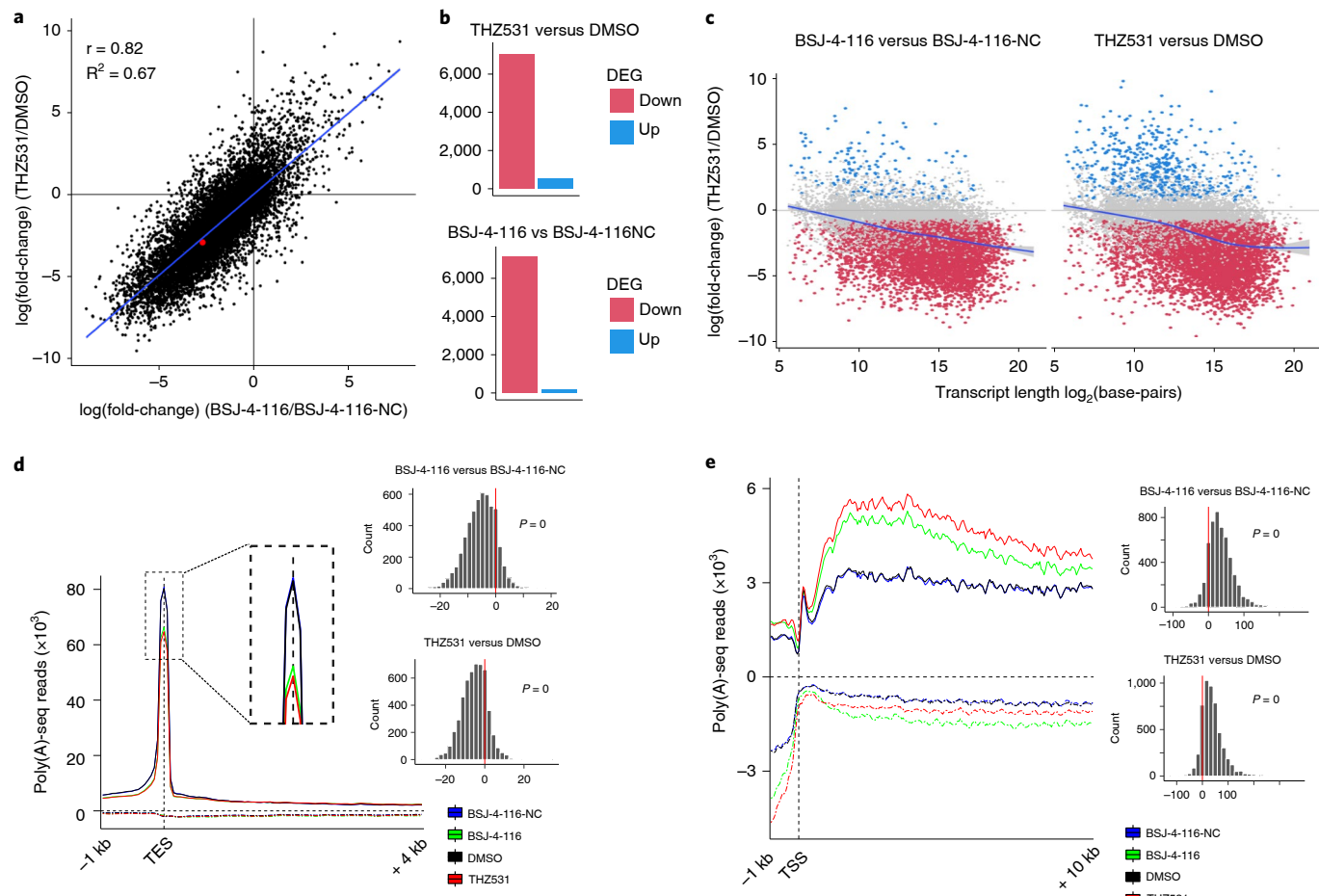


Fig. 2 | CDK12 degradation preferentially leads to premature cleavage and poly(adenylation) of long genes enriched with DDR genes. **a**, Scatter plot showing $\log_2(\text{fold change})$ in gene expression in Jurkat cells treated with BSJ-4-116 (50 nM) versus THZ531 (250 nM) for 8 h. BSJ-4-116 and THZ531 datasets were normalized to BSJ-4-116-NC and DMSO, respectively. The red dot indicates CDK12. **b**, Quantification of differentially expressed genes (DEG) in conditions illustrated in **a**. **c**, Scatter plot showing $\log_2(\text{fold change})$ in gene expression versus gene length on a \log_2 scale for each protein-coding gene in cells treated as in **a**. **d**, Left: average metagene profiles of normalized poly(A) 3'-sequence reads at the TES (-1 to +4 kb) for all detected cells treated as in **a**. Right: Wilcoxon's test showing significant shift in reads in BSJ-4-116- and THZ531-treated cells ($P = 0$). **e**, Left: average metagene profiles of normalized poly(A) 3'-sequence reads at the TSS (-1 to +10 kb) for all detected cells treated as in **a**. Right: Wilcoxon's test showing a significant shift in read distribution toward positive in BSJ-4-116- and THZ531-treated cells ($P = 0$).

levels (Fig. 2a), with 7,050 and 7,123 downregulated transcripts (false discovery rate (FDR) $<= 0.01$), respectively (Fig. 2b). Overall, 115 upregulated transcripts and 6,021 downregulated transcripts were shared between BSJ-4-116 and THZ531 treatments (Extended Data Fig. 2c). In contrast, direct pairwise comparison between BSJ-4-116- and THZ531-treated cells or between BSJ-4-116-NC and dimethyl sulfoxide (DMSO) control cells, showed only 211 genes (1.5% of total) and 1 gene differentially expressed, respectively. Gene set enrichment analysis (GSEA) demonstrated that genes involved in DDR pathway-related processes were negatively enriched on treatment with BSJ-4-116, with double-strand break repair as the most negatively enriched process (Extended Data Fig. 2d). For BSJ-4-116, there were two additional hits: transfer RNA metabolic process and regulation of GTPase activity (Extended Data Fig. 2e and Supplementary Dataset 3). This result is in line with the known enrichment for DDR genes with genetic perturbation of CDK12 or with THZ531 treatment (Extended Data Fig. 2f)^{12,13,26}. Furthermore, the downregulation of DDR-related genes was evident at the mRNA level with 10 h of treatment and protein level by 24 h and, accordingly, we observed an increase in γ -H2AX, a marker of DNA damage, and apoptosis markers (Extended Data Fig. 2f).

Mechanistically, recent studies demonstrated that DDR genes under CDK12 regulation are enriched for specific genetic characteristics, such as increased gene length and low U1:poly(adenylation) site (PAS) ratio, which makes them more susceptible to premature cleavage and poly(adenylation). In the present study, we noted that transcriptional downregulation observed with both BSJ-4-116 and THZ531 treatment was indeed associated with increased gene length (Fig. 2c). Next, to evaluate whether BSJ-4-116 treatment also causes poly(adenylation), we focused on identifying poly(A) peaks associated with known upstream PAS motifs (Extended Data Fig. 2g). A metagene analysis of the distribution of poly(A) 3'-sequence reads, for all protein-coding genes across the genome, revealed that BSJ-4-116 and THZ531, but not BSJ-4-116-NC or DMSO, elicited significant loss of annotated terminal or 3'-poly(A) sites (Fig. 2d and Extended Data Fig. 2h), and an increase in poly(adenylated) sites at the 5'-proximal ends of genes (Fig. 2e and Extended Data Fig. 2h). This observation could be attributed to a shift from the usage of canonical PAS within the 3'-UTR, and exonic poly(adenylation) sites to PAS within intronic regions at the 5'-end (Extended Data Fig. 2i). Taken together, our data showed that a selective, CDK12 small-molecule degrader, BSJ-04-116, preferentially downregulated

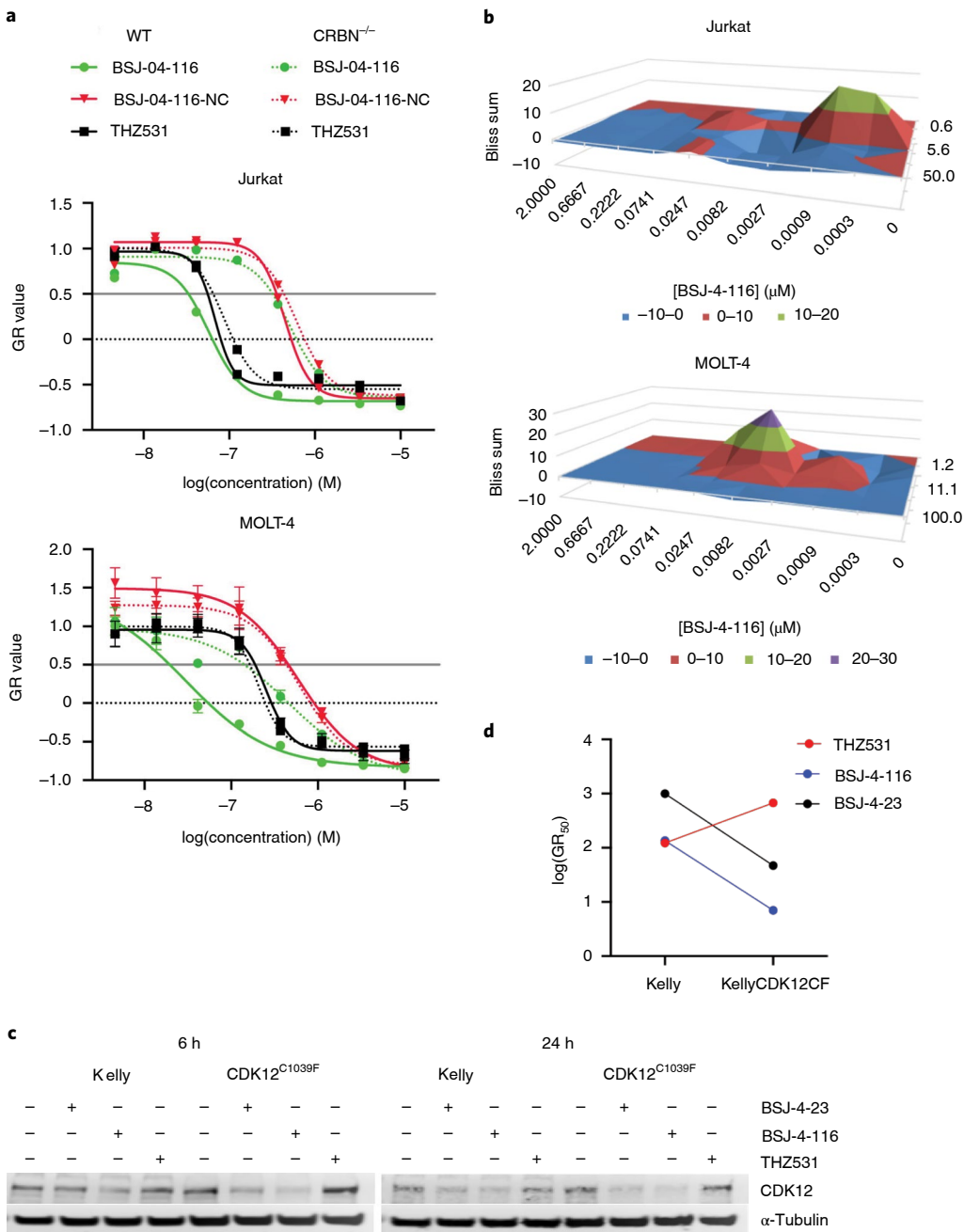


Fig. 3 | BSJ-4-116 inhibits the growth of T-ALL cells and sensitizes them to PARP inhibition. **a**, Dose-response curves for WT and CCRN-null Jurkat (top) and WT and CCRN-null MOLT-4 (bottom) cells treated with BSJ-4-116, BSJ-4-116-NC or THZ531 at indicated dose range for 72 h. Percentage cell growth relative to DMSO-treated cells was analyzed using a GR assay method (see Methods for details). Data are presented as mean \pm s.d. of $n=3$ biologically independent samples and represent $n=2$ independent experiments. **b**, Excess over Bliss synergy plots for serial dilutions of BSJ-4-116 in combination with olaparib in Jurkat (top) and MOLT-4 (bottom) cells. Excess of Bliss score sum >0 indicates synergistic interaction ($n=3$ replicates). **c**, Immunoblots for CDK12 and GAPDH in parental and CDK12^{C1039F} (KellyCDK12CF)-expressing Kelly cells treated with DMSO or BSJ-4-23 (250 nM) or BSJ-4-116 (50 nM) for 6 h and 24 h, respectively. Data represent $n=2$ independent experiments. **d**, Dot plot depicting relative antiproliferative activity of BSJ-4-116, BSJ-4-23 and THZ531 in parental Kelly and KellyCDK12CF cells. The GR₅₀ values were obtained using the same protocol as in **a**.

DDR genes by increasing poly(adenylation), which resulted in early transcriptional termination, in line with previous results obtained using dual CDK12/-13 inhibitor THZ531 (Extended Data Fig. 2j)^{12,13}. This suggests that CDK12 alone is necessary and sufficient to suppress the use of cryptic intronic poly(adenylation) sites.

BSJ-4-116 synergizes with PARP inhibitor in T-ALL cells. To establish the growth rate inhibition (GR) profile of the degrader

molecule, we conducted experiments using BSJ-4-116, THZ531 and BSJ-04-116-NC in wild-type (WT) T-ALL cell lines (Jurkat and MOLT-4), as well as CRBN^{-/-} cells, which were used to assess CRBN-independent effects. The 3-d GR assays⁴⁰ were performed to evaluate sensitivity to CDK12 inhibition and degradation. BSJ-4-116 treatment resulted in comparable or lower 50% GR (GR_{50}) values than THZ531 in WT T-ALL cells (Fig. 3a). Importantly, BSJ-4-116-NC was tenfold less potent than BSJ-4-116, indicating

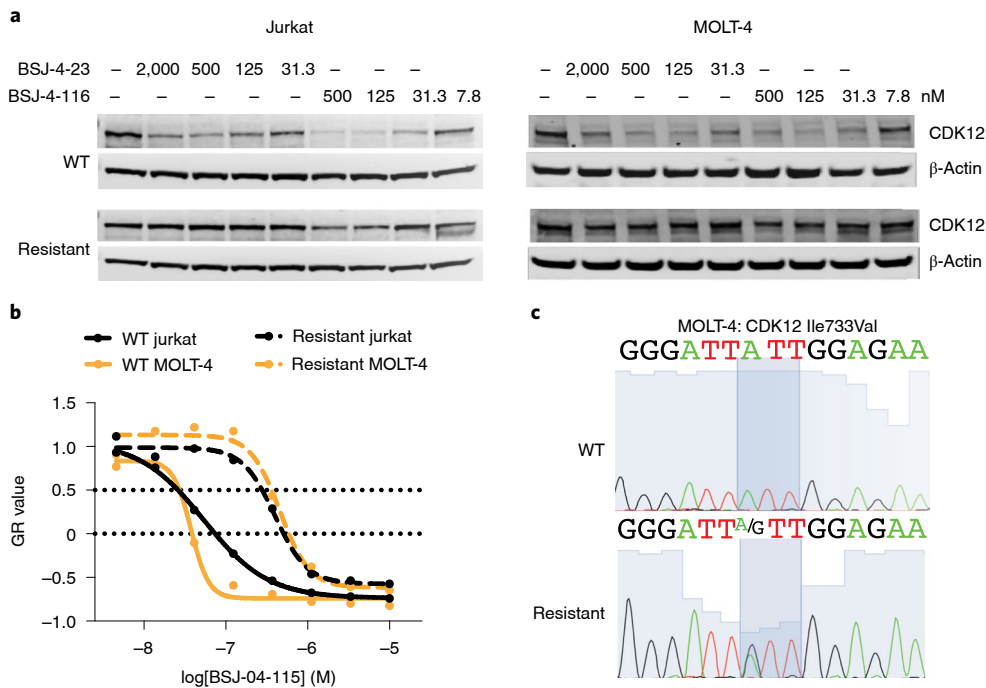


Fig. 4 | Chronic exposure leads to acquired resistance to BSJ-4-116 mediated by G-loop mutations. **a**, Immunoblots for CDK12 and GPADH in parental and resistant Jurkat and MOLT-4 cells treated with BSJ-4-116 and BSJ-4-23, at the indicated concentrations for 6 h. Data represent $n=2$ independent experiments. **b**, Dose-response curves for parental and resistant Jurkat and MOLT-4 cells treated with BSJ-4-116 at the indicated dose range for 72 h. Data are presented as mean \pm s.d. of $n=3$ biologically independent samples and represent $n=2$ independent experiments. **c**, Detection of heterozygous Ile733Val mutation in MOLT-4-resistant cells. DNA chromatograms of Sanger sequencing show the region of mutation from PCR-amplified CDK12 complementary DNA.

CDK12 degradation as the main mode of action. This was further supported by the observation that CRBN^{-/-} cells displayed pronounced resistance to BSJ-4-116, while responding similarly to BSJ-4-116-NC and THZ531 (Fig. 3a). Similar to THZ531, BSJ-4-116, but not BSJ-4-116-NC, caused accumulation of G2/M cells (Extended Data Fig. 3a). Given that BSJ-4-116 was observed to downregulate transcription of genes involved in DDR pathways, we examined whether treatment with the degrader molecule sensitizes T-ALL cells to PARP inhibition. To examine the impact of CDK12 degradation and DDR inhibition, we combined BSJ-4-116 with a PARP inhibitor, olaparib, in WT Jurkat and MOLT-4 cells. A strong synergistic interaction was observed as demonstrated by Bliss sum calculations (Fig. 3b). Such synergy was not observed in CRBN^{-/-} cells (Extended Data Fig. 3b). Taken together, we demonstrate that the selective CDK12 degradation alone or in combination with a PARP inhibitor has strong growth inhibitory effects in T-ALL cell lines.

BSJ-4-116 overcomes CDK12^{C1039F} mutation. One of the potential advantages of degrader molecules is their ability to overcome drug resistance given their unique ternary complex formation and degradation-based mechanism of action. To assess the ability of BSJ-4-116 to inhibit the growth of drug-resistant cell lines, we took advantage of neuroblastoma Kelly cells (KellyCDK12CF) that acquired CDK12^{C1039F} as a resistant mutation during chronic exposure to E9, a covalent kinase inhibitor directed at Cys1039 (ref. ²⁰). We treated parental and CDK12^{C1039F} Kelly cells with BSJ-4-23, BSJ-4-116 or THZ531 for 6 h and 24 h, using DMSO treatment as a negative control. Addition of the degrader molecule led to the same level of CDK12 protein level decrease, regardless of the mutational status of the cell line (Fig. 3c). Moreover, antiproliferative activity of BSJ-4-116 and BSJ-4-23, but not THZ531, was also independent of the

mutational status, and the degrader compounds exhibited improved GR₅₀ values in Kelly CDK12^{C1039F} cells compared with the parental cell line (Fig. 3d). Altogether, BSJ-4-116 represents a CDK12 chemical degrader with superior potency and selectivity than currently available small-molecule inhibitors.

CDK12 mutations lead to degrader resistance. Although capable of overcoming resistance to inhibitors as shown above and previously^{30–32}, degrader molecules may also lead to acquired resistance. However, the mechanisms of degrader-acquired resistance have yet to be fully characterized. In addition to our interest in mechanisms behind acquired resistance to degraders, we have recently demonstrated that chronic selection of resistance can be used to target deconvolution and validation²⁰. In the present study, to ultimately validate CDK12 as the target for the cell growth inhibition phenotype of BSJ-4-116 and further build on our understanding of the mechanisms of acquired resistance to bifunctional degraders, we exposed MOLT-4 and Jurkat cells to increasing doses of BSJ-4-116 until they repopulated at a normal rate under constant exposure to 0.5 μ M BSJ-4-116, approximately tenfold of its GR₅₀ in parental cells. As shown in Fig. 4a, in the presence of BSJ-4-116 or BSJ-4-23, the resistant cells retained CDK12 levels equivalent to those observed in parental cells treated with DMSO control. Resistant cells accordingly displayed a marked increase from 26 nM to 366 nM in GR₅₀ (Fig. 4b and Extended Data Fig. 4a). To determine whether a loss of CDK12 engagement through mutation might have occurred, we first performed Sanger sequencing of the CDK12 kinase domain in MOLT-4-resistant cells and identified that CDK12 harbors a heterozygous point mutation Ile733Val (Fig. 4c). To test the effect of this point mutation, we prepared recombinant Ile733Val CDK12 and subjected it to in vitro kinase assays. These assays revealed that Ile733Val conferred a slight gain of kinase activity, as well as loss of

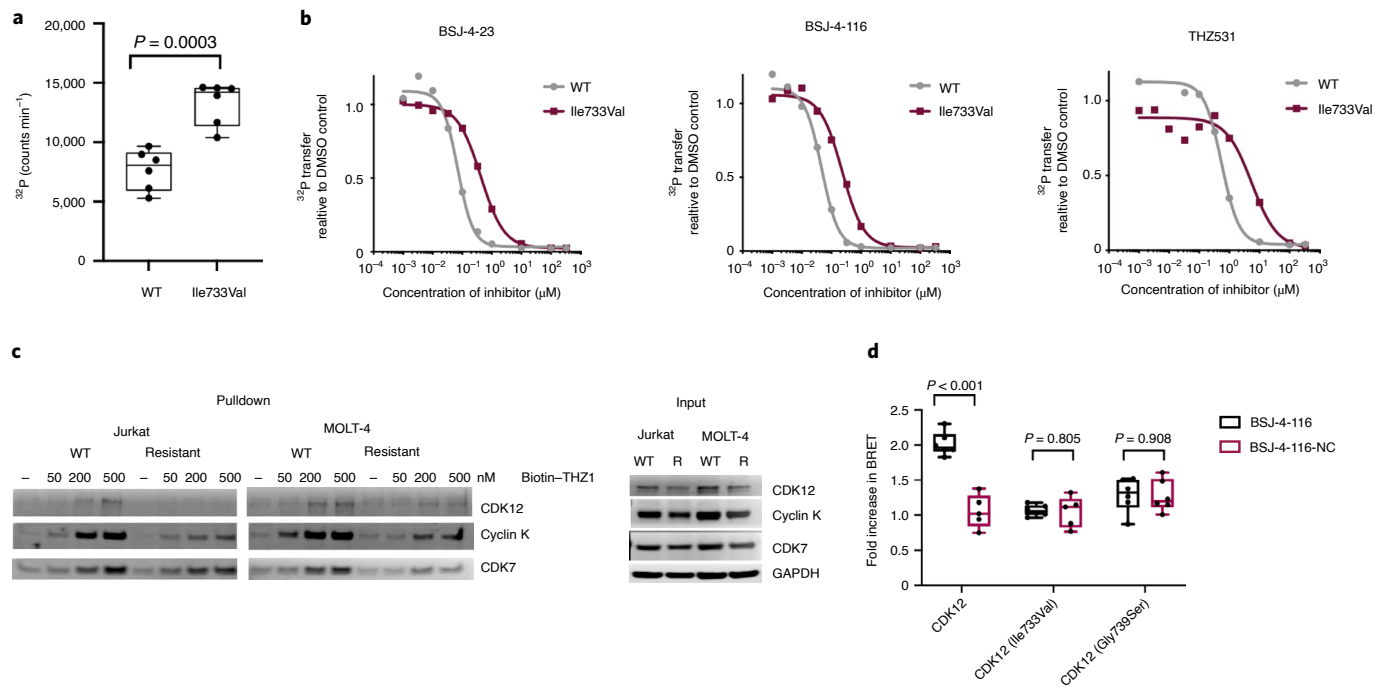


Fig. 5 | Chronic exposure leads to acquired resistance to BSJ-4-116 mediated by G-loop mutations. **a,b**, The ^{32}P -labeled ATP CDK12^{WT/Mut} kinase assay. CDK12^{Ile733V} displayed increased kinase activity (**a**) and was less efficiently targetable with all compounds tested compared with WT CDK12 (**b**). **c**, Pulldown assays for CDK12 or cyclin K and CDK7 with biotin-THZ1 at indicated doses from parental or resistant Jurkat and MOLT-4 cells. Immunoblots showing the relative capacity of THZ1 to enrich CDK12 (or cyclin K as a common surrogate) and CDK7 in parental and resistant (R) cells. Total protein, 25 μg , was loaded as a control for basal expression of CDK12, cyclin K and CDK7, and GAPDH expression. Data represent $n=2$ independent experiments. **d**, NanoBRET, live-cell ternary complex assays performed in MOLT-4 cells co-expressing HaloTag-CRBN and one of the following C-terminal NanoLuc fusions: CDK12, CDK12 (Ile733Val) or CDK12 (Gly739Ser). The fold increase in NanoBRET signal relative to BSJ-4-116-NC was plotted after 3 h of treatment with the indicated compounds. Data in **a**, **b** and **d** are presented as mean \pm s.d. of $n=6$ biologically independent samples and represent $n=2$ independent experiments.

binding affinity with BSJ-4-23, BSJ-4-116 and THZ531 (Fig. 5a,b). Subsequently, a single-cell clone of Jurkat-resistant cells was subjected to whole-exome sequencing. Among the approximately nonsynonymous exonic 200 mutations, excluding loss-of-function variants in resistant Jurkat cells that did not exist in parental cells (Supplementary Dataset 1), a single heterozygous point mutation Gly739Ser in CDK12 was identified and subsequently confirmed with Sanger sequencing (Extended Data Fig. 4b). To our surprise, resistant cells remained equally sensitive to a recently developed CDK9 degrader THAL-SNS-032 (ref. ²⁷) (Extended Data Fig. 4c), further confirming that CRBN-mediated proteasome machinery was still functional. It is of interest that Gly739 and Ile733 are located in the highly conserved glycine-rich loop in the kinase domain that mediates ATP alignment and binding (Extended Data Fig. 4d)⁴¹. This prompted us to examine the binding capacity of a previously developed CDK7/-12/-13 covalent inhibitor, THZ1, linked to biotin, via pulldown assays¹⁹. The lysate from either parental or resistant Jurkat cells was treated with biotin-THZ1, enriched on streptavidin-agarose beads and analyzed by western blotting to examine the protein levels. As shown in Fig. 5c, biotin-THZ1 dose dependently enriched CDK12 as well as cyclin K (commonly used as a surrogate marker for CDK12 binding), both of which were entirely lost in resistant counterparts. In contrast, CDK7, as another covalent target of THZ1, displayed no differential enrichment in parental versus resistant cell lines. To examine the impact of these mutants on ternary complex formation, we performed NanoBRET live-cell ternary complex assays in MOLT-4 cells transiently co-expressing HaloTag-CRBN and one of the following C-terminal NanoLuc

fusions—CDK12, CDK12 (Ile733Val) or CDK12 (Gly739Ser)—to monitor the CRBN engagement in MOLT-4 cells. The fold increase in NanoBRET signal relative to a DMSO control was plotted after 3-h treatment with the indicated compounds with $n=6$ technical replicates. A robust ternary complex was induced between CDK12 and CRBN with BSJ-4-116, but not with BSJ-4-116-NC. No appreciable ternary complex formation was observed between CDK12-resistant mutants with CRBN, indicating that those evolving mutations can prevent ternary complex formation at a molecular level, which is needed for degradation by our CDK12 degraders (Fig. 5d). This phenomenon strongly suggests the loss of direct degrader binding due to G-loop mutations as a mechanism for acquired resistance.

Discussion

CDK12 and its close homolog CDK13 are transcriptional CDKs, and individual genetic deletion of each leads to downregulation of distinct subsets of genes^{13,26}. DDR genes are preferentially sensitive to CDK12 deletion, which opens up a therapeutic potential for CDK12 inhibitors as treatments for cancers that harbor a proficient DDR function, such as those overexpressing *BRCA1/-2*. However, development of pharmacological agents that are selective for CDK12 over CDK13 has not been achieved^{19,22,23}. Degrader molecules present a novel pharmacological modality of chemical protein knockdown that has been shown to exhibit improved selectivity relative to parental inhibitors^{27,38}. To discover a selective CDK12 degrader, we employed computational modeling and ligand efficiency calculations⁴² as criteria for guiding degrader design, resulting in identification of fragment 5 as a privileged scaffold for selective CDK12

degradation. The computational analysis of the potential ternary complex between CDK12 and CRBN unveiled several features of CDK12 that we exploited to achieve selectivity over CDK13. As we show, fragment 5 takes advantage of the differences between the residues that are responsible for stabilizing PPIs, and the differences between intrinsic conformational flexibility for CDK12 and CDK13. Our modeling of fragment 5, a new CDK12 binder derived from THZ531, and BSJ-4-23, a selective CDK12 degrader, identified the importance of the exit vector (*R*)-3-aminopiperidine in BSJ-4-23. Thus, guided by this finding, we were able to rationally design a highly potent and selective CDK12 degrader BSJ-4-116 by replacing the exit vector of TL12-86 with (*R*)-3-aminopiperidine. Using a range of *in vitro* and cell-based experiments, we validated BSJ-4-116 as the first CDK12-selective compound. Using BSJ-4-116 as a tool compound, we unambiguously validated the role of CDK12 in transcriptional regulation. For example, BSJ-4-116 downregulated DDR genes through a premature termination of transcription, primarily through increasing poly(adenylation). The results we report in the present study, together with recently published studies^{12,13}, strongly support the view that CDK12 activity is necessary and sufficient to suppress the use of cryptic intronic poly(adenylation) sites. Although there are other reported redundant functions of CDK12 and CDK13 (refs. ^{24,43}), a different cellular context might play a role for their functions and our selective compounds could be helpful in delineating the functions in more detail.

In terms of potential application of CDK12-selective degraders as a therapeutic strategy, the results we obtained in the present study using T-ALL cell lines suggest that CDK12 degraders alone, or in combination with PARP inhibitors, may offer a therapeutically relevant opportunity. Importantly, CDK12 degraders may be especially relevant to overcome the drug-resistant CDK12 phenotypes characterized by an acquired Cys1039Phe mutation^{13,20}. Having said that, similar to what has been seen for many other therapies, and especially small-molecule-based inhibitors, prolonged (chronic) dosing with degraders may also result in acquired resistance phenotypes. Thus far, few reported cases that examined this possibility suggested that cells acquire resistance to degrader molecules by changing the composition of the E3 ligase complexes to exclude the E3 subunit that is essential for degrader binding, such as CRBN⁴⁴. In the present study, we report another mechanism for acquired resistance that involves emergence of the mutations on the target protein. More specifically, we document that chronic exposure of MOLT-4 and Jurkat cells to BSJ-4-116 led to the development of resistance to CDK12 degradation via point mutations on CDK12. We identified that two specific mutations on CDK12's G-loop, Ile733Val and Gly739Ser, give rise to the observed resistance. It is interesting that we observed that an Ile733Val mutation both reduces BSJ-4-116 binding and enhances CDK12 kinase activity, which together reduce the efficacy of the compound. In addition, cellular target engagement assays suggest that both mutants reduced not only CDK12-binding affinity for the degrader molecule but also affinity for the covalent inhibitor THZ1, while retaining an intact CRBN complex. Thus, to our knowledge, BSJ-4-116 represents the first example of resistance to a bivalent degrader molecule that is a consequence of an acquired point mutation in the target protein.

Online content

Any methods, additional references, Nature Research reporting summaries, source data, extended data, supplementary information, acknowledgements, peer review information; details of author contributions and competing interests; and statements of data and code availability are available at <https://doi.org/10.1038/s41589-021-00765-y>.

Received: 15 May 2020; Accepted: 4 February 2021;

Published online: 22 March 2021

References

- Hydbring, P., Malumbres, M. & Sicinski, P. Non-canonical functions of cell cycle cyclins and cyclin-dependent kinases. *Nat. Rev. Mol. Cell Biol.* **17**, 280–292 (2016).
- Shiekhattar, R. et al. Cdk-activating kinase complex is a component of human transcription factor TFIIFH. *Nature* **374**, 283–287 (1995).
- Fisher, R. P. Secrets of a double agent: CDK7 in cell-cycle control and transcription. *J. Cell Sci.* **118**, 5171–5180 (2005).
- Galbraith, M. D., Bender, H. & Espinosa, J. M. Therapeutic targeting of transcriptional cyclin-dependent kinases. *Transcription* **10**, 118–136 (2019).
- Gajduskova, P. et al. CDK11 is required for transcription of replication-dependent histone genes. *Nat. Struct. Mol. Biol.* <https://doi.org/10.1038/s41594-020-0406-8> (2020).
- Ramanathan, Y. et al. Three RNA polymerase II carboxyl-terminal domain kinases display distinct substrate preferences. *J. Biol. Chem.* **276**, 10913–10920 (2001).
- Davidson, L., Muniz, L. & West, S. 3' end formation of pre-mRNA and phosphorylation of Ser2 on the RNA polymerase II CTD are reciprocally coupled in human cells. *Genes Dev.* **28**, 342–356 (2014).
- Bartkowiak, B. et al. CDK12 is a transcription elongation-associated CTD kinase, the metazoan ortholog of yeast Ctk1. *Genes Dev.* **24**, 2303–2316 (2010).
- Blazek, D. et al. The cyclin K/Cdk12 complex maintains genomic stability via regulation of expression of DNA damage response genes. *Genes Dev.* **25**, 2158–2172 (2011).
- Li, X., Chatterjee, N., Spirohn, K., Boutros, M. & Bohmann, D. Cdk12 is a gene-selective RNA polymerase II kinase that regulates a subset of the transcriptome, including Nrf2 target genes. *Sci. Rep.* **6**, 21455 (2016).
- Iniguez, A. B. et al. EWS/FLI confers tumor cell synthetic lethality to CDK12 inhibition in Ewing sarcoma. *Cancer Cell* **33**, 202–216.e6 (2018).
- Dubbury, S. J., Boutz, P. L. & Sharp, P. A. CDK12 regulates DNA repair genes by suppressing intronic polyadenylation. *Nature* **564**, 141–145 (2018).
- Krajewska, M. et al. CDK12 loss in cancer cells affects DNA damage response genes through premature cleavage and polyadenylation. *Nat. Commun.* **10**, 1757 (2019).
- Negrini, S., Gorgoulis, V. G. & Halazonetis, T. D. Genomic instability—an evolving hallmark of cancer. *Nat. Rev. Mol. Cell Biol.* **11**, 220–228 (2010).
- Lui, G. Y. L., Grandori, C. & Kemp, C. J. CDK12: an emerging therapeutic target for cancer. *J. Clin. Pathol.* **71**, 957–962 (2018).
- Bayles, I. et al. Ex vivo screen identifies CDK12 as a metastatic vulnerability in osteosarcoma. *J. Clin. Invest.* **129**, 4377–4392 (2019).
- Bradner, J. E., Hnisz, D. & Young, R. A. Transcriptional addiction in cancer. *Cell* **168**, 629–643 (2017).
- Paculova, H. et al. *BRCA1* or CDK12 loss sensitizes cells to CHK1 inhibitors. *Tumour Biol.* **39**, 1010428317727479 (2017).
- Zhang, T. et al. Covalent targeting of remote cysteine residues to develop CDK12 and CDK13 inhibitors. *Nat. Chem. Biol.* **12**, 876–884 (2016).
- Gao, Y. et al. Overcoming resistance to the THZ series of covalent transcriptional CDK inhibitors. *Cell Chem. Biol.* **25**, 135–142 e135 (2018).
- Johannes, J. W. et al. Structure-based design of selective noncovalent CDK12 inhibitors. *ChemMedChem* **13**, 231–235 (2018).
- Ito, M. et al. Discovery of 3-benzyl-1-(trans-4-((5-cyanopyridin-2-yl)amino)cyclohexyl)-1-arylurea derivatives as novel and selective cyclin-dependent kinase 12 (CDK12) inhibitors. *J. Med. Chem.* **61**, 7710–7728 (2018).
- Quereda, V. et al. Therapeutic targeting of CDK12/CDK13 in triple-negative breast cancer. *Cancer Cell* **36**, 545–558 e547 (2019).
- Fan, Z. et al. CDK13 cooperates with CDK12 to control global RNA polymerase II processivity. *Sci. Adv.* **6**, <https://doi.org/10.1126/sciadv.aaz5041> (2020).
- Liang, K. et al. Characterization of human cyclin-dependent kinase 12 (CDK12) and CDK13 complexes in C-terminal domain phosphorylation, gene transcription, and RNA processing. *Mol. Cell Biol.* **35**, 928–938 (2015).
- Greifenberg, A. K. et al. Structural and functional analysis of the Cdk13/cyclin K complex. *Cell Rep.* **14**, 320–331 (2016).
- Olson, C. M. et al. Pharmacological perturbation of CDK9 using selective CDK9 inhibition or degradation. *Nat. Chem. Biol.* **14**, 163–170 (2018).
- Jiang, B. et al. Development of dual and selective degraders of cyclin-dependent kinases 4 and 6. *Angew. Chem. Int. Ed. Engl.* **58**, 6321–6326 (2019).
- Brand, M. et al. Homolog-selective degradation as a strategy to probe the function of CDK6 in AML. *Cell Chem. Biol.* **26**, 300–306 e309 (2019).
- Salami, J. et al. Androgen receptor degradation by the proteolysis-targeting chimera ARCC-4 outperforms enzalutamide in cellular models of prostate cancer drug resistance. *Commun. Biol.* **1**, 100 (2018).
- Sun, Y. et al. Degradation of Bruton's tyrosine kinase mutants by PROTACs for potential treatment of ibrutinib-resistant non-Hodgkin lymphomas. *Leukemia* **33**, 2105–2110 (2019).
- Dobrovolsky, D. et al. Bruton tyrosine kinase degradation as a therapeutic strategy for cancer. *Blood* **133**, 952–961 (2019).

33. Cooper, J. M. et al. Overcoming BET inhibitor resistance in malignant peripheral nerve sheath tumors. *Clin. Cancer Res.* **25**, 3404–3416 (2019).
34. Cheng, M. et al. Discovery of potent and selective epidermal growth factor receptor (EGFR) bifunctional small-molecule degraders. *J. Med. Chem.* **63**, 1216–1232 (2020).
35. Burslem, G. M. & Crews, C. M. Small-molecule modulation of protein homeostasis. *Chem. Rev.* **117**, 11269–11301 (2017).
36. Watt, G. F., Scott-Stevens, P. & Gaohua, L. Targeted protein degradation in vivo with proteolysis targeting chimeras: current status and future considerations. *Drug Discov. Today Technol.* **31**, 69–80 (2019).
37. Burslem, G. M. & Crews, C. M. Proteolysis-targeting chimeras as therapeutics and tools for biological discovery. *Cell* **181**, 102–114 (2020).
38. Huang, H. T. et al. A chemoproteomic approach to query the degradable kinome using a multi-kinase degrader. *Cell Chem. Biol.* **25**, 88–99.e6 (2018).
39. Choi, S. H. et al. CDK12 phosphorylates 4E-BP1 to enable mTORC1-dependent translation and mitotic genome stability. *Genes Dev.* **33**, 418–435 (2019).
40. Hafner, M., Niepel, M., Chung, M. & Sorger, P. K. Growth rate inhibition metrics correct for confounders in measuring sensitivity to cancer drugs. *Nat. Methods* **13**, 521–527 (2016).
41. Bosken, C. A. et al. The structure and substrate specificity of human Cdk12/cyclin K. *Nat. Commun.* **5**, 3505 (2014).
42. Hopkins, A. L., Groom, C. R. & Alex, A. Ligand efficiency: a useful metric for lead selection. *Drug Discov. Today* **9**, 430–431 (2004).
43. Chirackal Manavalan, A. P. et al. CDK12 controls G1/S progression by regulating RNAPII processivity at core DNA replication genes. *EMBO Rep.* **20**, e47592 (2019).
44. Zhang, L., Riley-Gillis, B., Vijay, P. & Shen, Y. Acquired resistance to BET-PROTACs (proteolysis-targeting chimeras) caused by genomic alterations in core components of E3 ligase complexes. *Mol. Cancer Ther.* **18**, 1302–1311 (2019).

Publisher's note Springer Nature remains neutral with regard to jurisdictional claims in published maps and institutional affiliations.

© The Author(s), under exclusive licence to Springer Nature America, Inc. 2021

Methods

Chemistry. Chemical synthesis and characterization are provided as a Supplementary Note.

Molecular docking. *Fragment docking.* Fragments were docked into CDK12 co-crystal structure (PDB accession no. 5ACB), ATP-binding pocket using an induced-fit protocol from Schrodinger's suite (v.2019 release 4). A standard protein preparation protocol was carried out before docking. Hinge hydrogen bonds with a MET816 backbone were used as a constraint to ensure the proper binding mode. Default values were adopted for other parameters. Ligand efficiency (LE) is defined as follows:

$$\text{LE} = \text{Glidescore}/(\text{Number of heavy atoms})$$

CRBN–CDK12 complex model prediction. Protein–protein docking by Rosetta (v.3.9) was used to generate ternary complex models of CDK12 and CRBN. The co-crystal structure of CRBN with lenalidomide (PDB accession no. 4TZ4) and fragment 5 in CDK12 (PDB accession no. 5ACB) were prepared for docking using the protein preparation protocol in Schrodinger's suite, and then followed by a standard Rosetta protein–protein docking procedure. Flat-bottomed harmonic constraint was applied to the amine nitrogen off the benzene ring and the piperidine nitrogen in fragment 5 for biasing the conformations within the range of practical degrader synthesis and reasonable molecular mass. The parameters were $x0=9$, $sd=1$ and $tol=7$ (https://www.rosettacommons.org/docs/latest/rosetta_basics/file_types/constraint-file). This constraint imposed no bias if the distance between the two nitrogen atoms was between 2 and 16 Å (0.2 and 1.6 nm), and harmonic energy would be added if the distance were outside the range. The range covered both close contact and reasonable linker length for forming ternary complexes. The sampling parameters for docking were ‘-ex1 -ex2aro -dock_pert 3 8’ with constraint specified. The 15,000 CRBN–CDK12 complex structures were generated, and 1,500 top conformations chosen for further analysis based on interface scores and satisfactory distance constraint. The top conformations were clustered by root-mean-square deviation of CDK12 backbone heavy atoms as a measure of conformational diversity. Then, 80 clusters were generated using Schrödinger's conformational clustering tool. The top conformation based on the interface score was chosen as the ternary complex model with $I_{sc} = -26.18$. The structure belonged to a cluster with 16 members and many of them ranked in the top scoring complexes (4 out of 10).

Docking of degrader BSJ-4-23. BSJ-4-23 was docked into the predicted CRBN and CDK12 complex model using the MOE (release 2019) template-docking protocol. The glutarimide in the CRBN-binding pocket and aminopyrimidine in the CDK12-binding site were chosen as the templates. Default values were used for docking parameters and proteins were kept rigid during docking calculations. The top scored pose was further refined by the protein–ligand complex refinement protocol in Schrodinger's suite.

Cell culture. Human T-ALL cell lines Jurkat and MOLT-4 were obtained from American Type Culture Collection (ATCC). The cells were tested for *Mycoplasma* spp. routinely using MycoAlert *Mycoplasma* detection kit (Lonza, catalog no. LT07-318). All cell lines used in the present study were maintained in RPMI-1640 medium (Thermo Fisher Scientific, catalog no. 11875119) supplemented with 10% fetal bovine serum (FBS; Gibco) at 37 °C in a humidified chamber in the presence of 5% CO₂.

Western blotting. The cells were collected by trypsinization and washed with phosphate-buffered saline (PBS). Cell lysates were prepared by using NP-40 lysis buffer (Invitrogen) supplemented with complete protease inhibitor cocktail (Roche), PhosSTOP phosphatase inhibitor cocktail (Roche) and phenylmethylsulfonyl fluoride (1 mM). The lysates were cleared by centrifugation and resolved using Bolt 4–12% Bis–Tris plus gels and underwent western blotting to detect proteins of interest. Antibodies used against various proteins were as follows: CDK12 (1:1,000, Cell Signaling Technologies, catalog no. 11973), CDK13 (1:2,000, Bethyl Laboratories, catalog no. A301-458A), BRCA1 (1:1,000, Cell Signaling Technologies, catalog no. 9010), BRCA2 (1:1,000, Cell Signaling Technologies, catalog no. 10741), cleaved PARP (1:1,000, Cell Signaling Technologies, catalog no. 5625), cleaved caspase 3 (1:1,000, Cell Signaling Technologies, catalog no. 9661), α-tubulin (1:4,000, Cell Signaling Technologies, catalog no. 3873), glyceraldehyde 3-phosphate dehydrogenase (GAPDH; 1:4,000, Cell Signaling Technologies, catalog no. 2118), RAD51 (1:1,000, Santa Cruz Biotechnologies, catalog no. sc-8349), anti-phospho-RNAPII antibody (Ser2; 1:1,000, Sigma-Aldrich, catalog no. 04-1571-I), anti-phospho-RNAPII antibody (Thr4; 1:1,000, Sigma-Aldrich, catalog no. MABE348), anti-phospho-RNAPII antibody (Ser5; 1:1,000, Sigma-Aldrich, catalog no. 04-1572-I), anti-phospho-RNAPII antibody (Ser7; 1:1,000, Sigma-Aldrich, catalog no. 04-1570-I) and RNAPII (1:1,000, Cell Signaling Technologies, catalog no. 14958). Antibodies were used according to the manufacturers' instructions. For visualization of western blots, Odyssey Clx (Li-cor) was utilized.

Proteomics. Methods described below were based on a reported protocol⁴⁵. Cells were rinsed once with 1× sterile PBS and stored at –80 °C. Cells were lysed by addition of sodium dodecylsulfate (SDS) lysis buffer (2% SDS, 150 mM NaCl, 50 mM Tris, pH 8.7) containing protease and phosphatase inhibitors (Halt Protease and Phosphatase Inhibitor Single-Use Cocktail, EDTA Free, Thermo Fisher Scientific, catalog no. 78441). Lysate was then pipetted on to Qiashredder filters (QIAGEN, ref. 79656) and centrifuged at maximum speed for 2 min at room temperature. Filtrate was collected and placed into a microfuge tube.

Disulfide reduction was performed by adding dithiothreitol to a final concentration of 5 mM and heating to 37 °C for 1 h, followed by alkylation with iodoacetamide at a final concentration of 15 mM, incubation at room temperature in the dark for 30 min and quenching with 50 mM freshly prepared dithiothreitol. Protein concentration was determined using a Micro BCA Protein Assay Kit (Thermo Fisher Scientific, catalog no. 23235) following the manufacturer's protocol. For each sample, an aliquot corresponding to 150 µg of total protein was withdrawn. Detergent was removed by methanol/chloroform protein precipitation as described previously⁴⁶. Precipitates were solubilized in freshly prepared 8 M urea in 200 mM EPPS (N-(2-hydroxyethyl)piperazine-N'-(3-propanesulfonic acid)), pH 8.5 and 60 µg of solubilized total protein from each sample was then used for tandem mass tag (TMT) labeling. After a 10-min incubation at 37 °C, the urea concentration was diluted with 200 mM EPPS to 2 M final concentration, 2% acetonitrile (v:v) was added and digestion was performed by overnight incubation at room temperature in the presence of Lys-C protease (Wako, catalog no. 129-02541) at an enzyme:substrate ratio of 1:75. After further dilution of the sample with 200 mM EPPS to a final urea concentration of 0.8 M in the presence of 2% acetonitrile (v:v), digestion was performed by incubation at 37 °C for 6 h with trypsin (Promega, catalog no. V5113) at an enzyme:substrate ratio of 1:75.

Digest check. The missed cleavage rate was determined by liquid chromatography (LC)–MS/MS. Total protein, 1 µg, was withdrawn from each sample and combined into a single sample. Only samples with a missed cleavage rate <10% were processed further.

TMT labeling, ratio check and HPLC fractionation. Equal amounts of protein were removed from each sample and labeled using a TMT11plex Mass Tag Labeling Kit (Thermo Fisher Scientific, catalog no. A34808). TMT labeling efficiency and ratio checks were measured by LC–MS/MS analysis of a combined 11-plex sample after combining equal volumes (about 1 µg) from each sample. Equal amounts of labeled peptide from each sample (as judged from the ratio check data) were then combined for subsequent analysis.

Quenching of TMT-labeling reactions was performed by adding hydroxylamine to a final concentration of 0.5% (v:v) and incubating samples for 10 min at room temperature. Formic acid (FA) was added to a final volume of 2% (v:v) to lower the pH to <3.0 and samples were combined and de-salted using a SepPak tC18 Vac RC Cartridge (50 mg, Waters, catalog no. WAT054960). High-performance LC (HPLC) fractionation was performed using an Agilent 1200 series instrument with a flow rate of 600 µl min⁻¹ over a period of 75 min. Peptides were collected in a 96-well plate over a 65-min gradient of 13–44% buffer B, with buffer A comprising 5% acetonitrile and 10 mM ammonium bicarbonate, pH 8 and buffer B comprising 90% acetonitrile and 10 mM ammonium bicarbonate, pH 8. Fractions were then pooled into 24 samples, followed by sample clean-up using the Stage Tip protocol. This protocol uses C18 Empore Extraction Disks (Thermo Fisher Scientific, catalog no. 14-386-2). The matrix was primed with methanol and equilibrated with 70% acetonitrile and 1% FA, followed by washing twice with 1% FA, loading the sample in 1% FA, followed once again by two 1% FA washes, and finally peptide elution using 70% acetonitrile and 1% FA. Samples were dried before resuspension in MS loading buffer (3% acetonitrile, 5% FA).

LC–MS. Peptides were injected on to a 30-cm, 100-µm (internal diameter) column and separated using an EASY-nLC 1200 HPLC (Thermo Fisher Scientific, catalog no. LC120). The flow rate was 450 nl min⁻¹ with a gradient of 6–28% buffer B over 170 min, with buffer A comprising 3% acetonitrile and 0.4% FA and buffer B comprising 100% acetonitrile and 0.4% FA. The column was packed with 1.8-µm C18 beads with a pore size of 12 nm (Sepax Technologies Inc.) heated to 60 °C using a column heater (constructed in-house). Samples from the HPLC were injected into an Orbitrap Fusion Lumos Tribrid MS (Thermo Fisher Scientific, catalog no. FSN02-10000) using a multi-notch MS3 method^{47,48}. MS scans were performed in the Orbitrap over a scan range of 400–1,400 m/z with dynamic exclusion. The top ten ions with charge states from two to six were selected for MS–MS. Rapid rate scans were performed in the ion trap with a collision energy of 35% and a maximum injection time of 120 ms. TMT quantification was performed using SPS-MS3 in the Orbitrap with a scan range of 100–1,000 m/z and a higher-energy collisional dissociation of 55%. Orbitrap resolution was 50,000 (dimensionless units) with a maximum injection time of 150 ms. MS isolation windows varied depending on the charge state. Further details on LC and MS parameters and settings used were described recently⁴⁹.

Proteomics data analysis. A compilation of commercially available software (Core software program) was used to convert MS data (Thermo ‘.RAW’ files) to

mzXML format and to correct monoisotopic *m/z* measurements and erroneous peptide charge state assignments. Assignment of MS–MS spectra was performed using the Sequest⁵⁰ (v.28; http://fields.scripps.edu/yates/wp/?page_id=17) and the Human UniProt database (downloaded February 2014). The database search included reversed protein sequences and known contaminants such as human keratins, which were excluded for subsequent analyses. Linear discriminant analysis was used to distinguish forward and reverse hits⁵¹. Peptides were identified using an MS2 spectrum and an FDR < 1% and was achieved by applying the target-decoy database search strategy. Filtering was performed as described previously⁴⁸. Variable extents of modification, including the presence of oxidized methionine and over-labeling of TMT on serine, threonine and tyrosine¹³, were considered during peptide assignment for whole-protein experiments. For protein identification and quantification, shared peptides were collapsed into the minimally sufficient number of proteins using rules of parsimony. Peptides with a total TMT value > 200 and an isolation specificity > 0.7 were included for quantification.

Cell viability assay. For 72-h viability assays using a GR method, cells were plated in 96-well plates at 6×10^3 cells per well for 24 h. Subsequently, time 0 was measured before cells were treated with a test compound at doses ranging from 10 nM to 10 μ M for 72 h. The number of viable cells was determined using the CellTiter-Glo Luminescent Cell Time 0 and time 72 h, dose range and corresponding luminescence intensity were uploaded to the GR₅₀ calculator (<http://www.grcalculator.org/grcalculator/>) to generate GR values, GR₅₀ and GR_{max}. GraphPad Prism v.8.0 (GraphPad Software Inc.) was used to plot dose-response curves.

FACS. For cell cycle analysis, cells (0.5×10^6) were treated with the test compounds at indicated concentrations for 24 h. The cells were dispensed with ice-cold 70% ethanol and subsequently fixed at -20°C , treated with RNase A (0.5 mg ml⁻¹) and stained with propidium iodide (50 $\mu\text{g ml}^{-1}$) until analysis. Samples were analyzed on a LSRFortessa cell analyzer (BD Biosciences) using BD FACSDiva. A minimum of 5×10^4 events was counted per sample for analysis. Data were analyzed using FlowJo software.

Reverse transcription-PCR. Total RNA was isolated with the RNAeasy Mini kit (QIAGEN). Purified RNA, 1 μg , was reverse transcribed using Superscript III First-Strand (Invitrogen) with random hexamer primers following the manufacturer's protocol. Quantitative PCR was carried out using the QuantiFast SYBR Green PCR kit (QIAGEN) and analyzed on an Applied Biosystems StepOne Real-Time PCR System (Life Technologies). Each individual biological sample was quantitative PCR amplified in technical triplicate and normalized to GAPDH as an internal control. Relative quantification was calculated according to the $\Delta\Delta C_t$ relative quantification method. Error bars indicate $\pm\text{s.d.}$ of three replicates. Primers sequences are available on request.

Poly(A) 3'-processing and analysis were performed as in Krajewska et al. with some minor modifications and summarized below¹³. For poly(A) 3'-end sequencing, Jurkat cells were exposed to DMSO or THZ531 (250 nM) or to BSJ-4-116 or BSJ-4-116-NC (50 nM) for 8 h. RNA extraction was performed with TRIzol (Ambion) following the manufacturer's instructions. Total RNA was treated with DNase I (Invitrogen). Sequencing libraries were prepared with the RNA-sequencing library kit (QuantSeq 3' mRNA Sequencing REV, Lexogen) following the manufacturer's instructions. All samples were sequenced on a HiSeq 2500 sequencer.

Poly(A) 3'-sequencing data processing. For each sample, single-end 100-bp reads were obtained and filtered using bbduk.sh from BBMap (v.37.00) and parameters ‘k=13 ktrim=r useshortkmers=t mink=5 qtrim=r trimq=20 minlength=75 ref=true seq_rna.fa.gz’ to remove potential adapter contamination or low-quality reads. High-quality reads were subsequently mapped to the human genome (GRCh38) with STAR (v.STAR_2.5.1b_modified) and the following parameters: ‘--outFilterType BySJout --outFilterMultimapNmax 20 --alignSJoverhangMin 8 --alignSJDBoverhangMin 1 --outFilterMismatchNmax 999 --outFilterMismatchNoverLmax 0.1 --alignIntronMin 20 --alignIntronMax 1000000 --alignMatesGapMax 1000000 --outSAMattributes NH HI NM MD --outSAMtype BAM SortedByCoordinate’. To create strand-specific sample coverage profiles in 50-bp bins, we used bamCoverage (DeepTools v.2.5.4) with parameters ‘--normalizeUsingRPKM -filterRNAstrand –bs 50’. Genome-wide correlation of biological replicates was calculated using Spearman's rank coefficient and visualized using scatterplots and heatmaps. These results showed high reproducibility for each condition and, hence, for all visualizations, replicates were merged using samtools merge and processed again as described for the individual replicates. ERCC spike-in sequences were added and used to compute sample-specific size factors to allow the detection of absolute gene expression level differences.

Poly(A) 3'-sequencing peak identification and filtering. Poly(A) sequencing peaks were called using MACS2 (v.2.1.1) and parameters ‘--nomodel --extsize 100 --shift 0’ using a merged bam file of all samples. To identify false-positive

poly(A) peaks, two criteria were used: (1) the presence of the potential PAS motifs (AATAAA, ATTAAA, AGTAAA, TATAAA, AATATA, AATACA, CATAAA, GATAAA, AATGAA, ACTAAA, AAGAAA, AATAGA) computed in a 100-bp window upstream of the peak in a strand-specific manner, and (2) the presence of a genomic 25-adenine stretch with a maximum of 3 mismatches computed in a 50-bp window downstream of the peak in a strand-specific manner. Peaks were removed if they were not associated with a PAS motif, but were associated with a genomic stretch of As. Retained poly(A) sequencing peaks were annotated in a stepwise manner: first, peaks were considered to be associated with the 3'-UTR if they were within the vicinity of the transcription end site (TES, -200 to $+600$ bp); next, the remaining peaks were considered to be intergenic or genic and, in the latter case, overlapping with an exon or intron. If a peak overlapped multiple transcripts, priority was given to protein-coding transcripts followed by longer transcripts. For metagene plots, genes were represented by the isoform that showed the highest combined 3'-UTR expression level.

Metagene profiles. A gene metaprofile was created by dividing each gene (from transcription start site (TSS) to TES) into 50 equally sized bins; 2 kb upstream and downstream flanking regions were binned in bins of 100 bp. Bedgraph files with normalized reads from TT-sequencing or poly(A) 3'-sequencing were used to calculate read density (reads per million per bp) across those bins and subsequently summarized for all genes. To create a TSS or TES metaprofile, we followed an analogous approach with variable upstream and downstream flanking regions and summarized bins of 50 bp. To compare TT-sequencing and poly(A) 3'-sequencing profiles, calculated read densities were rescaled between 1 and 100.

Correlation of transcript length and 3' expression changes. To identify differentially expressed genes based on poly(A) 3'-sequencing, all counts for 3'-UTR-associated poly(adenylation) sites were summarized per gene. This data matrix was log₂(normalized) and used to identify differential expression and fold changes with the limma package in R. Correlation between fold changes and transcript length was performed on the highest expressed transcript for each gene in the control condition. A generalized additive model smoothing curve was fitted to each treatment to observe global changes and for visualization purposes.

Intronic poly(adenylation) usage. For each transcript (transcripts per million > 1) the reads of all intronic and 3'-UTR-associated poly(A) sites were summarized. To compare the change and usage of intronic versus 3'-UTR-associated poly(A) sites between different treatments, an odds ratio was calculated for each treatment sample, but excluding transcripts that had no intronic poly(A) sites in either treatment. A two-sample Kolmogorov–Smirnov test was then used to detect changes in odds ratio distributions between different treatments.

Enrichment analysis. GSEA for gene sets of biological processes was performed using the GSEA preranked tool from the Broad Institute.

Whole-exome sequencing. Both parental and resistant clones of Jurkat cells were sent to Novogene for whole-exome sequencing with duplicates. Sequencing libraries were generated by Agilent sureselect human all exon v.6 kit. Then, 8.3-G data were obtained for each sample on average with quality value ≥ 30 of 92.5%. Sequencing data was trimmed using cutadapt (<https://cutadapt.readthedocs.io/en/stable>) with ‘-q 20, 20 -m 90 -trim-n’ to remove adapters and low-quality reads. BWA-mem (<http://bio-bwa.sourceforge.net>) was used to align the reads to human reference genome hg.19. Duplicating reads were marked by picard Markduplicates (<https://broadinstitute.github.io/picard>). GATK (<https://gatk.broadinstitute.org/hc/en-us>) was used to do indel realignment and subsequent mutations calls with mutect2. Variants were filtered by Filtermutectcalls with ‘max_events-in-region 5’ and ‘false-discovery-rate 0.01’. Other parameters used in GATK calls were default. Variant annotation was carried out using Annovar (<https://annovar.openbioinformatics.org/en/latest/>). Loss-of-function mutations such as frameshift and stop gain were removed. Nonsynonymous exonic point mutations were kept. Mutations with average read depth < 10 or in genomic duplication region (that is, genomicSuperDups > 95%) were also removed from further analysis. In addition, only mutations with allele frequency > 25% in resistant cells were kept.

In vitro CDK12 kinase assay. WT CDK12 kinase assay. This assay was performed by Reaction Biology Corporation according to standard methods with minor modifications to the reported protocol. Briefly, compounds were tested in 12-point dose-response, at a maximum concentration of 10 μM . Assays were performed at an ATP concentration of 30 μM (K_m) CDK12/cyclin K.

Mutated CDK12 kinase assay. Recombinant GST-CDK12 (714-1063)/GST-cyclin K (1-267) was co-expressed with Cdk-activating kinase from *Saccharomyces cerevisiae* in Sf9 insect cells using the MultiBacTurbo system⁵². Site-directed mutagenesis was used to generate CDK12 point mutations (Ile733Val).

After expression for 72 h, cells were harvested by centrifugation. Cells were resuspended in lysis buffer (50 mM 4-(2-hydroxyethyl)-1-piperazine-ethanesulfonic acid (Hepes), pH 7.4, 300 mM NaCl, 5% glycerol and 5 mM 2-mercaptoethanol) and disrupted by sonication. After centrifugation

in a Beckman Avanti J-26S XP with a JA-25.50 rotor (20,000 r.p.m. for 45 min at 10 °C), lysate was applied to GST Trap FF columns (GE Healthcare) equilibrated with lysis buffer using an Äkta Prime chromatography system (GE Healthcare), followed by extensive washes with 10 column volumes of lysis buffer. Proteins were eluted in elution buffer (50 mM Hepes, pH 7.4, 300 mM NaCl, 5% glycerol, 5 mM 2-mercaptoethanol and 10 mM glutathione) and incubated overnight with tobacco etch virus protease for tag cleavage. Size exclusion chromatography on a Superdex 200 PG column (GE Healthcare) was used to further purify the complex using size exclusion chromatography buffer (200 mM Hepes, pH 7.4, 150 mM NaCl, 5% glycerol and 1 mM tris(2-carboxyethyl)phosphine). Fractions of the main peak were analyzed by SDS–polyacrylamide gel electrophoresis and stoichiometric kinase complex was pooled and concentrated using Amicon filters (Millipore). Proteins were aliquoted, snap frozen in liquid nitrogen and stored at –80 °C.

Radioactive kinase activity measurements were performed using 0.2 mM [γ -³²P]ATP containing 0.45 mCi of ³²P per ml (Perkin Elmer). CDK12/cyclin K complexes were preincubated at 0.2 μ M with varying concentrations of compound for 5 min at 30 °C, followed by addition of substrate and an additional incubation for 15 min at 30 °C. Reactions were stopped by ethylenediaminetetraacetic acid (EDTA), added to a final concentration of 50 mM. Mixtures were spotted on to filter sheets of Amersham Protran nitrocellulose membrane (GE Healthcare) and washed three times for 5 min with 0.75% (v:v) phosphoric acid. Radioactivity was counted in a Beckman Liquid Scintillation Counter (Beckman-Coulter) for 1 min.

NanoBRET ternary complex experiments. MOLT-4 cells (ATCC) were grown and maintained in RPMI-1640 medium (Gibco) supplemented with 10% FBS (Seradigm) before performing experiments. Then, 2×10^6 cells were electroporated with 2 μ g of total plasmid DNA per reaction, consisting of one of each of the following CDK proteins: full-length human CDK12 (Uniprot, catalog no. Q9NYV4), CDK12 (Ile733Val), CDK12 (Gly739Ser), CDK12 (Lys745Arg), CDK12 (Leu752Met), CDK12 (Lys745Arg/Leu752Met) or full-length CDK13 (Uniprot, catalog no. Q14004), CDK13 Arg723Lys, CDK13 Met730L and CDK13 Arg723Lys/Met730Leu fused at the C terminus with NanoLuc in combination with HaloTag–CRBN at a 1:10 donor (NanoLuc):acceptor (HaloTag) DNA ratio. Reactions were assembled in 100- μ l volume using the Amaxa Cell Line Nucleofector Kit L (Lonza), and pulsed using the Nucleofector 2b Device (Lonza) and program C-005. After electroporation, cells were incubated in growth medium in a six-well plate for 24 h at 37 °C and 5% CO₂ before plating 3.5×10^3 cells per well into 96-well, white assay plates in the presence and absence of HaloTag NanoBRET 618 ligand (Promega) and 30 nM BSJ-4-116 or BSJ-4-116-NC compounds. After a 3-h incubation at 37 °C and 5% CO₂, NanoBRET NanoGlo substrate (Promega) was added to the plate, and dual filtered luminescence was collected using a CLARIOstar plate reader (BMG Labtech) equipped with a 460/80-nm bandpass filter and a 610-nm long-pass filter (acceptor, HaloTag NanoBRET ligand) using an integration time of 0.5 s. Background-subtracted NanoBRET ratios expressed in milliBRET units were calculated from the following equation:

$$\text{mBRET ratio} = \left(\frac{\text{Acceptor channel}}{\text{Donor channel}} - \frac{\text{Acceptor channel (no ligand)}}{\text{Donor channel (no ligand)}} \right) \times 1,000$$

Fold increase in BRET was calculated by normalizing the mBRET ratios to the average mBRET ratios for negative control BSJ-4-116-NC.

Quantification and statistical analysis. Data are presented as the mean \pm s.d. of a minimum of three experiments, except where indicated. Student's *t*-test (two tailed, unpaired) was used to compare the means for two groups, whereas one-way analysis of variance was used in comparisons with multiple groups. Analyses were performed with GraphPad Prism v.7.02 (GraphPad Software Inc.). *P* < 0.05 was considered significant. No data were excluded.

Reporting Summary. Further information on research design is available in the Nature Research Reporting Summary linked to this article.

Data availability

Dataset of exonic nonsynonymous variants excluding loss-of-function mutations in Jurkat-resistant cells is available in Supplementary Dataset 1. KINOMEscan data are provided in Supplementary Dataset 2. A complete GSEA result is provided in Supplementary Dataset 3. Whole-exome sequencing data of parental and resistant cell lines to BSJ-4-116 have been deposited at the National Center for Biotechnology Information (NCBI) Sequence Read Archive with BioProject

accession no. PRJNA634900. Poly(A) 3'-sequencing data have been deposited at the NCBI's Gene Expression Omnibus (accession no. GSE161650). Crystal structure of human CRBN in complex with DDB1 and lenalidomide has a PDB accession no. 4TZ4. Crystal structures of the human CDK12–cyclin K complex have PDB accession nos. 5ACB, 6CKX and 6B3E. Crystal structure of the human CDK13–cyclin K complex has PDB accession no. 5EFQ. Source data are provided with this paper.

References

45. Song, Y. et al. A dynamic view of the proteomic landscape during differentiation of ReNcell VM cells, an immortalized human neural progenitor line. *Sci. Data* **6**, 190016 (2019).
46. Wessel, D. & Flügge, U. I. A method for the quantitative recovery of protein in dilute solution in the presence of detergents and lipids. *Anal. Biochem.* **138**, 141–143 (1984).
47. Ting, L., Rad, R., Gygi, S. P. & Haas, W. MS3 eliminates ratio distortion in isobaric multiplexed quantitative proteomics. *Nat. Methods* **8**, 937–940 (2011).
48. McAlister, G. C. et al. MultiNotch MS3 enables accurate, sensitive, and multiplexed detection of differential expression across cancer cell line proteomes. *Anal. Chem.* **86**, 7150–7158 (2014).
49. Paulo, J. A. et al. Quantitative mass spectrometry-based multiplexing compares the abundance of 5000 *S. cerevisiae* proteins across 10 carbon sources. *J. Proteomics* **148**, 85–93 (2016).
50. Eng, J. K., McCormack, A. L. & Yates, J. R. An approach to correlate tandem mass spectral data of peptides with amino acid sequences in a protein database. *J. Am. Soc. Mass. Spectrom.* **5**, 976–989 (1994).
51. Elias, J. E. & Gygi, S. P. Target-decoy search strategy for increased confidence in large-scale protein identifications by mass spectrometry. *Nat. Methods* **4**, 207–214 (2007).
52. Bienossek, C., Iimasaki, T., Takagi, Y. & Berger, I. MultiBac: expanding the research toolbox for multiprotein complexes. *Trends Biochem. Sci.* **37**, 49–57 (2012).

Acknowledgements

We thank M. Kostic for her editing of this manuscript. This work was supported by a National Institutes of Health grant (nos. P01 CA154303 to N.S.G. and U24-DK116204 to P.K.S.) and Deutsche Forschungsgemeinschaft GE 976/9-2 (to M.K.).

Author contributions

N.S.G. and T.Z. conceived the project. B.J. performed the compound synthesis and structure determination with help from I.Y. Y.G. and W.L. executed cellular biological experimental research with help from J.J. K.R. and D.D. performed the NanoBRET ternary complex assays. J.C. executed computational modeling, whole-exome sequencing analysis and mutational experiments design. R.D. and Y.G. performed genomic data analysis. I.K and M.G. executed CDK12 *in vitro* kinase assay. M.B. M.K. and P.K.S. performed proteomic analysis. T.Z. Y.G. J.C. B.J. and N.S.G. co-wrote the paper. All authors edited the manuscript.

Competing interests

N.S.G. is a founder, science advisory board member and equity holder in Gatekeeper, Syros, Petra, C4, B2S, Aduro and Soltego. The Gray lab receives or has received research funding from Novartis, Takeda, Astellas, Taiho, Janssen, Kinogen, Voronoi, Her2llc, Deerfield, Epiphanes and Sanofi. J.C. is a consultant to Soltego, Jengu and Allorion, and equity holder for Soltego, Allorion and M3 bioinformatics & technology Inc. P.K.S. is a member of the science advisory board or board of directors of Merrimack Pharmaceutical, Glencoe Software, Applied Biomath and RareCyte Inc., and has equity in these companies. B.J., J.C., Y.G., N.K., T.Z. and N.S.G. are inventors on CDK12 degrader patents. All remaining authors declare no competing interests.

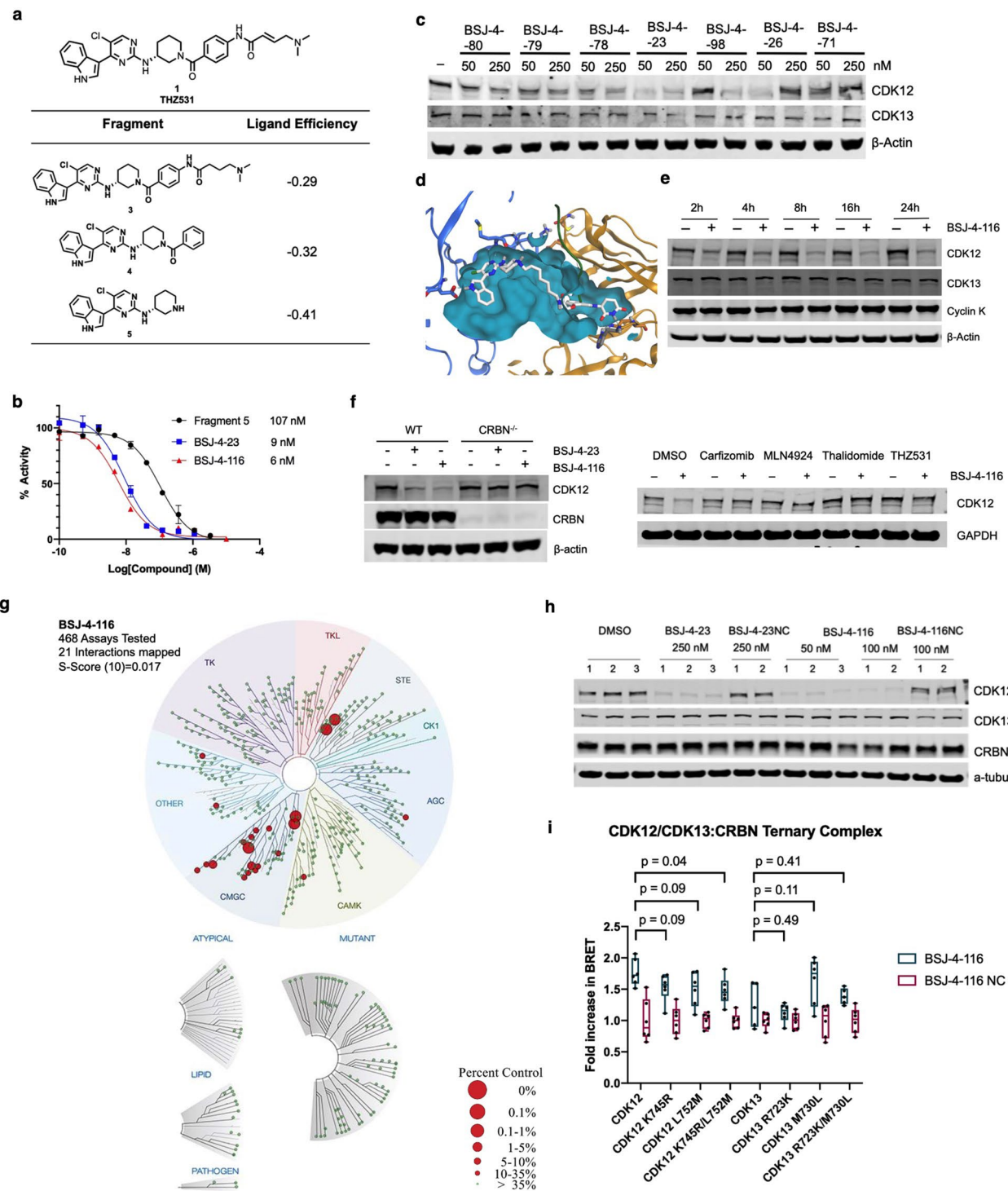
Additional information

Extended data is available for this paper at <https://doi.org/10.1038/s41589-021-00765-y>.

Supplementary information The online version contains supplementary material available at <https://doi.org/10.1038/s41589-021-00765-y>.

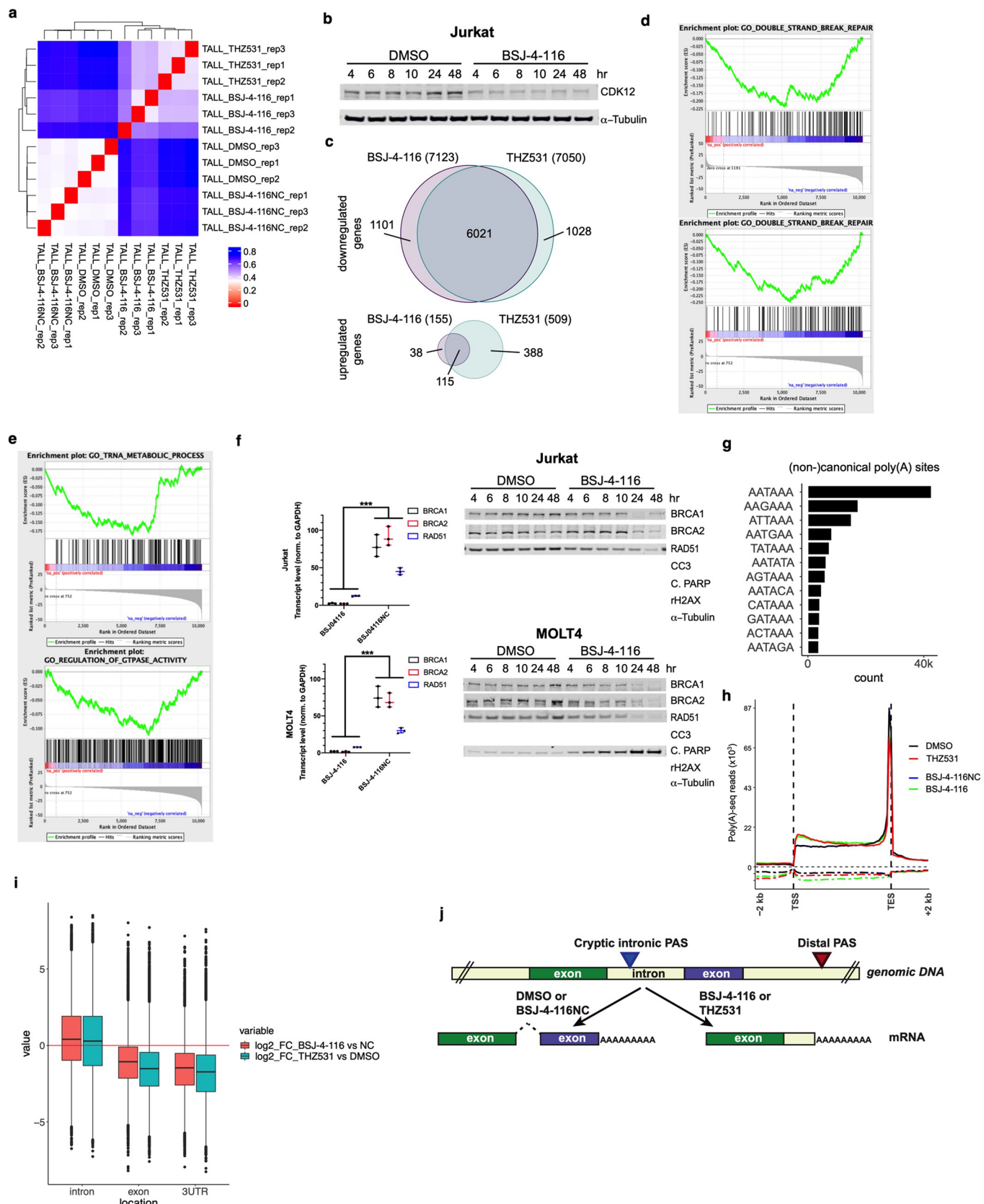
Correspondence and requests for materials should be addressed to T.Z. or N.S.G.

Reprints and permissions information is available at www.nature.com/reprints.



Extended Data Fig. 1 | See next page for caption.

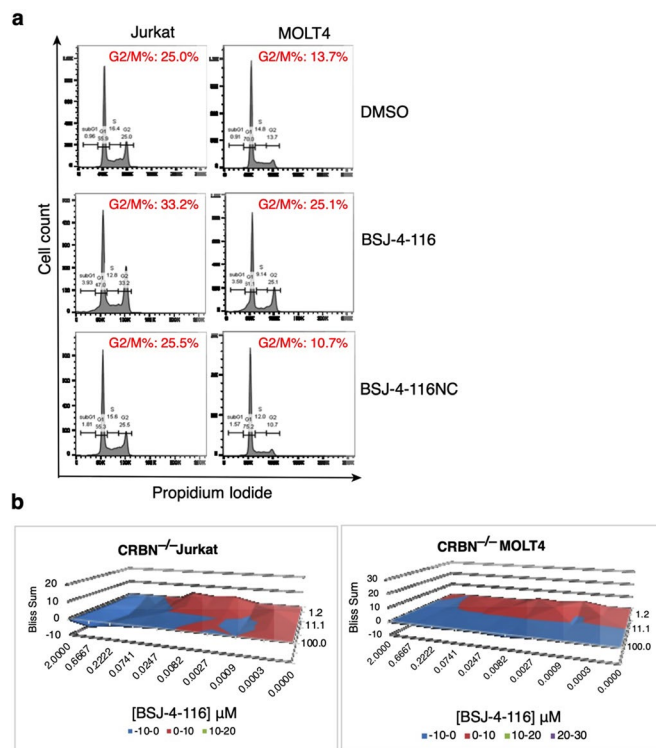
Extended Data Fig. 1 | Development of CDK12 degraders BSJ-4-23 and BSJ-4-116. **a**, Chemical structures of THZ531 and its 3 fragments with ligand efficiency values. **b**, *In vitro* CDK12 kinase assay. Assays were performed at an ATP concentration of 30 μ M (apparent Km). Data are presented as mean \pm s.d. of $n = 3$ biologically independent samples. **c**, Preliminary screening immunoblots for CDK12, CDK13 and β -Actin in Jurkat cells after 6 h treatment with DMSO or different CDK12 degraders at the indicated concentrations. **d**, Binding groove for BSJ-4-23 in modeled ternary complex of CDK12/BSJ-4-23/CRBN (CDK12 in blue, PDB ID: 5ACB, CRBN in orange, PDB ID: 4TZ4, BSJ-4-23 carbons in light grey). **e**, Time-dependent effect of BSJ-4-116 (50 nM) on CDK12, CDK13 and cyclin K protein levels after 2 h, 4 h, 8 h, 16 h and 24 h treatment in Jurkat cells. **f**, Left: Immunoblots for CDK12, CRBN and β -Actin in WT and CRBN null Jurkat cells after 6 h treatment with DMSO, BSJ-4-23 (250 nM) and BSJ-4-116 (50 nM); Right: Immunoblots for CDK12 and α -tubulin in Jurkat cells following 2 h pre-treatment with DMSO, Carfilzomib (400 nM), MLN4924 (1000 nM), Thalidomide (1000 nM) and THZ531 (250 nM) followed by 6 h co-treatment with DMSO or BSJ-4-116 (50 nM). **g**, KinomeScan kinase selectivity profile for BSJ-4-116. BSJ-4-116 was profiled at a concentration of 1 μ M against a panel of 468 human kinases. The results for the binding interactions are reported as a percent of the DMSO control (% control), where larger red circles indicate stronger binding hits. The selectivity score was defined as the ratio of the number of kinases inhibited to a specified percentage versus the total number of kinases. For this experiment, specified percent inhibition was set at 10%, resulting in S(10) value of 0.017 for BSJ-4-116. **h**, Degradation effect of BSJ-4-116 and BSJ-4-116NC at indicated doses prechecked by western blots for the proteomics experiment in Jurkat cells. Data in (c), (e), (f) and (h) represent $n=2$ independent experiments. **i**, NanoBRET live cell ternary complex assays performed in MOLT-4 cells co-expressing HaloTag-CRBN and one of the following C-terminal NanoLuc fusions: CDK12, CDK12 (K745R), CDK12 (L752M), CDK12 (K745R/L752M) or CDK13, CDK13 (R723K), CDK13 (M730L), CDK13 (R723K/M730L). The fold increase in NanoBRET signal relative to BSJ-4-116NC was plotted after 3 h treatment with the indicated compounds with $n=6$ biologically independent samples.



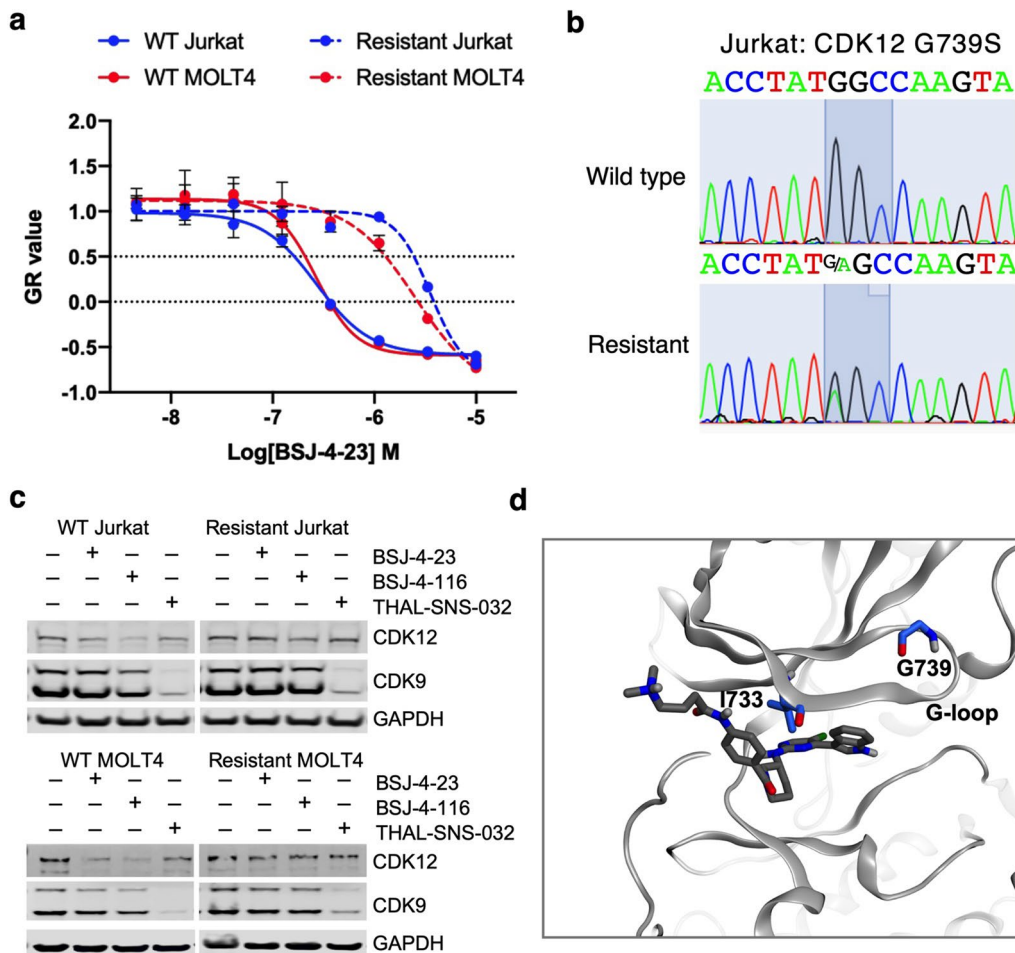
Extended Data Fig. 2 | See next page for caption.

Extended Data Fig. 2 | CDK12 degradation preferentially leads to premature cleavage and polyadenylation (PCPA) of long genes enriched with DDR genes.

a, Genome-wide correlation analysis for replicates from each condition showing significant correlation between BSJ-4-116 vs THZ531, and DMSO vs BSJ-4-116NC. **b**, Immunoblots for CDK12 and α -tubulin in Jurkat cells treated with DMSO or BSJ-4-116 (50 nM) for indicated hours. Data are representative of $n=2$ independent experiments. **c**, Fisher exact test showing significant overlap in genes downregulated by BSJ-4-116 vs THZ531 ($p=0$). There was also significant overlap in the small numbers of gene upregulated ($p=1.42e-136$). **d**, GSEA of downregulated genes in Jurkat cells treated with BSJ-4-116 and THZ531. **e**, Additional enriched GSEA signatures enriched by BSJ-4-116 treatment. **f**, Left: qRT-PCR analysis of the indicated DDR gene expression in Jurkat and MOLT4 cells treated with BSJ-4-116 (50 nM) or BSJ-4-116NC (100 nM) for 10 h. Data were normalized to GAPDH and compared to DMSO-treated controls ($n=3$). Right: Immunoblots for indicated DDR and cell death markers in Jurkat and MOLT4 cells treated with DMSO or BSJ-4-116 (50 nM) for indicated hours. Data are representative of $n=2$ independent experiments. **g**, Bar plot showing the frequency of retrieved polyadenylation site (PAS) motifs 100bp upstream of the poly(A) 3'-seq peaks. **h**, Average metagene profiles of normalized poly(A) 3'-seq reads over gene bodies and extending -2 to +2 kb of all detected genes in Jurkat cells treated with BSJ-4-116 (50 nM) or THZ531 (250 nM) vs DMSO for 8 h. Sense and antisense reads are depicted by solid and dashed lines, respectively. **i**, Boxplots showing the differential usage (log₂ fold-change) of polyadenylation sites at three different genomic locations. The comparison BSJ-4-116 vs. BSJ-4-116NC is shown in red and THZ531 vs. DMSO is shown in green. **j**, Schematic illustration of PCPA caused by CDK12 inhibition or degradation.



Extended Data Fig. 3 | BSJ-4-116 inhibits the growth of T-ALL cells and sensitizes them to PARP inhibition. **a**, Cell-cycle analysis of Jurkat and MOLT4 cells treated with BSJ-4-116 (50 nM) and BSJ-4-116NC (100 nM) for 24 h. DNA was stained with propidium iodide (PI) before flow cytometry analysis. G/M% values are presented as mean \pm s.d. of $n=3$ biologically independent samples and are representative of $n=2$ independent experiments. **b**, Excess over Bliss synergy plots for serial dilutions of BSJ-4-116 in combination with Olaparib in CCRN null Jurkat (top) and MOLT4 (bottom) cells. $n=3$ replicates.



Extended Data Fig. 4 | Chronic exposure leads to acquired resistance to BSJ-4-116 mediated by G-loop mutations. **a**, Dose response curves for parental and resistant Jurkat and MOLT4 cells treated with BSJ-4-23 at indicated dose range for 72 h. Percent cell growth relative to DMSO-treated was analyzed using growth rate inhibition assay method. Data are presented as mean \pm s.d. of n=3 biologically independent samples. **b**, Detection of heterozygous G739S mutation in Jurkat resistant cells. DNA chromatograms of sanger sequencing shows region of mutation from PCR-amplified CDK12 cDNA. **c**, Immunoblots for CDK12, CDK9 and GAPDH in parental and resistant Jurkat and MOLT4 cells treated with DMSO, BSJ-4-23 (250 nM), BSJ-4-116 (50 nM) or THAL-SNS-032 (250 nM) for 8 h. Data represent n=2 independent experiments. **d**, CDK12 kinase domain structure (PDB code: 5ACB) showing the locations of G-loop mutations I733 and G739.

Reporting Summary

Nature Research wishes to improve the reproducibility of the work that we publish. This form provides structure for consistency and transparency in reporting. For further information on Nature Research policies, see our [Editorial Policies](#) and the [Editorial Policy Checklist](#).

Statistics

For all statistical analyses, confirm that the following items are present in the figure legend, table legend, main text, or Methods section.

n/a Confirmed

- The exact sample size (n) for each experimental group/condition, given as a discrete number and unit of measurement
- A statement on whether measurements were taken from distinct samples or whether the same sample was measured repeatedly
- The statistical test(s) used AND whether they are one- or two-sided
Only common tests should be described solely by name; describe more complex techniques in the Methods section.
- A description of all covariates tested
- A description of any assumptions or corrections, such as tests of normality and adjustment for multiple comparisons
- A full description of the statistical parameters including central tendency (e.g. means) or other basic estimates (e.g. regression coefficient) AND variation (e.g. standard deviation) or associated estimates of uncertainty (e.g. confidence intervals)
- For null hypothesis testing, the test statistic (e.g. F , t , r) with confidence intervals, effect sizes, degrees of freedom and P value noted
Give P values as exact values whenever suitable.
- For Bayesian analysis, information on the choice of priors and Markov chain Monte Carlo settings
- For hierarchical and complex designs, identification of the appropriate level for tests and full reporting of outcomes
- Estimates of effect sizes (e.g. Cohen's d , Pearson's r), indicating how they were calculated

Our web collection on [statistics for biologists](#) contains articles on many of the points above.

Software and code

Policy information about [availability of computer code](#)

Data collection	Software used for data collection and analysis are listed below. Our own code can be received as indicated in the data availability statement section.
Data analysis	STAR (v2.5.1b), DeepTools (v2.5.4), Limma package (Deseq2), GraphPad Prism (v7.02), Schrodinger suite commercial software (v2019 release 4), Rosetta (v3.9), HiSeq 2500 sequencer (Illumina) and whole exome sequencing analysis was done using publicly available NGS software described in the manuscript.

For manuscripts utilizing custom algorithms or software that are central to the research but not yet described in published literature, software must be made available to editors and reviewers. We strongly encourage code deposition in a community repository (e.g. GitHub). See the Nature Research [guidelines for submitting code & software](#) for further information.

Data

Policy information about [availability of data](#)

All manuscripts must include a [data availability statement](#). This statement should provide the following information, where applicable:

- Accession codes, unique identifiers, or web links for publicly available datasets
- A list of figures that have associated raw data
- A description of any restrictions on data availability

Dataset of Exonic nonsynonymous variants excluding loss of function mutations in Jurkat resistant cells is available in Supplementary Dataset 1. KINOMEscan data is provided in Supplementary Dataset 2. Complete GSEA result is provided in Supplementary Dataset 3. Whole exome sequencing data of parental and resistant cell lines to BSJ-4-116 has been deposited to NCBI sequence read archive with BioProject ID PRJNA634900. Poly(A) 3'-sequencing data has been deposited to the NCBI GEO (accession number: GSE161650).

Field-specific reporting

Please select the one below that is the best fit for your research. If you are not sure, read the appropriate sections before making your selection.

Life sciences

Behavioural & social sciences Ecological, evolutionary & environmental sciences

For a reference copy of the document with all sections, see nature.com/documents/nr-reporting-summary-flat.pdf

Life sciences study design

All studies must disclose on these points even when the disclosure is negative.

Sample size	Sample sizes were not predetermined using statistical analyses. Sample sizes were selected based on prior experiences and common practice in this field. Information on the number of replicates and independent experiments that were performed for each measurement are disclosed in the manuscript.
Data exclusions	Data were not excluded from analysis.
Replication	All biological experiments were successfully reproduced in independent experiments. Commercial screening data was controlled for reproducibility by use of technical replicates and comparison of control molecules to reference data. Information on the number of replicates and independent experiments that were performed for each measurement are disclosed in the manuscript.
Randomization	Randomization was not applicable to this study.
Blinding	Blinding was not applicable to this study.

Reporting for specific materials, systems and methods

We require information from authors about some types of materials, experimental systems and methods used in many studies. Here, indicate whether each material, system or method listed is relevant to your study. If you are not sure if a list item applies to your research, read the appropriate section before selecting a response.

Materials & experimental systems

n/a	Involved in the study
<input type="checkbox"/>	<input checked="" type="checkbox"/> Antibodies
<input type="checkbox"/>	<input checked="" type="checkbox"/> Eukaryotic cell lines
<input checked="" type="checkbox"/>	<input type="checkbox"/> Palaeontology and archaeology
<input checked="" type="checkbox"/>	<input type="checkbox"/> Animals and other organisms
<input checked="" type="checkbox"/>	<input type="checkbox"/> Human research participants
<input checked="" type="checkbox"/>	<input type="checkbox"/> Clinical data
<input checked="" type="checkbox"/>	<input type="checkbox"/> Dual use research of concern

Methods

n/a	Involved in the study
<input type="checkbox"/>	<input checked="" type="checkbox"/> ChIP-seq
<input type="checkbox"/>	<input checked="" type="checkbox"/> Flow cytometry
<input checked="" type="checkbox"/>	<input type="checkbox"/> MRI-based neuroimaging

Antibodies

Antibodies used

Antibodies used against various proteins were as follows: CDK12 (1:1000, Cell Signaling Technologies #11973), CDK13 (1:2000, Bethyl Laboratories #A301-458A), BRCA1 (1:1000, Cell Signaling Technologies #9010), BRCA2 (1:1000, Cell Signaling Technologies #10741), cleaved PARP (1:1000, Cell Signaling Technologies #5625), cleaved caspase 3 (1:1000, Cell Signaling Technologies #9661), β -tubulin (1:4000, Cell Signaling Technologies #3873), GAPDH (1:4000, Cell Signaling Technologies #2118), RAD51 (1:1000, Santa Cruz Biotechnologies #sc-8349), Anti-phospho-RNAPII Antibody (Ser2) (1:1000, Sigma-Aldrich #04-1571-I), Anti-phospho-RNAPII Antibody (Thr4) (1:1000, Sigma-Aldrich #MABE348), Anti-phospho-RNAPII Antibody (Ser5) (1:1000, Sigma-Aldrich #04-1572-I), Anti-phospho-RNAPII Antibody (Ser7) (1:1000, Sigma-Aldrich #04-1570-I), RNAPII (1:1000, Cell Signaling Technologies #14958).

Validation

Antibodies were validated by the manufacturer according to standard protocols denoted on the manufacturer website.

Eukaryotic cell lines

Policy information about [cell lines](#)

Cell line source(s)

Human T-cell acute lymphoblastic leukemia cell lines Jurkat and MOLT4 (ATCC).

Authentication

Cell lines were originally purchased directly from the vendor. Authentication was performed by the vendor, which includes STR profiling. Additional authentication was not performed.

Mycoplasma contamination

All cell lines tested negative for mycoplasma.

Commonly misidentified lines
(See [ICLAC](#) register)

No commonly misidentified lines were used in this study.

Flow Cytometry

Plots

Confirm that:

- The axis labels state the marker and fluorochrome used (e.g. CD4-FITC).
- The axis scales are clearly visible. Include numbers along axes only for bottom left plot of group (a 'group' is an analysis of identical markers).
- All plots are contour plots with outliers or pseudocolor plots.
- A numerical value for number of cells or percentage (with statistics) is provided.

Methodology

Sample preparation

For cell cycle analysis, cells (0.5×10^6) were treated with the test compounds at indicated concentrations for 24 h. The cells were dispensed with ice-cold 70% ethanol and subsequently fixed at -20°C, treated with RNase A (0.5 mg/ml) and stained with propidium iodide (PI) (50 µg/ml) until analysis. Samples were analyzed on a LSRFortessaTM cell analyzer (BD Biosciences) using BD FACSDiva. A minimum of 5×10^4 events were counted per samples for analysis. Data were analyzed using FlowJo software.

Instrument

LSRFortessaTM cell analyzer (BD Biosciences), BD FACSDiva

Software

FlowJo software

Cell population abundance

For each set of experiments equal number of cells were evaluated. The total number of cells for each set of experiments are 50,000.

Gating strategy

Gates and regions are placed around cell population with special characteristics.

- Tick this box to confirm that a figure exemplifying the gating strategy is provided in the Supplementary Information.